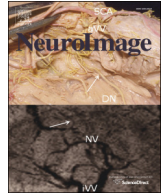




Contents lists available at ScienceDirect

NeuroImage

journal homepage: www.elsevier.com/locate/ynimg

Q1 Estimating anatomical trajectories with Bayesian mixed-effects modeling

Q2 G. Ziegler ^{a,b,*}, W.D. Penny ^a, G.R. Ridgway ^{a,c}, S. Ourselin ^{b,d}, K.J. Friston ^a,
3 for the Alzheimer's Disease Neuroimaging Initiative ¹

4 ^a Wellcome Trust Centre for Neuroimaging, Institute of Neurology, University College London, UK

5 ^b Dementia Research Centre, Institute of Neurology, University College London, UK

6 ^c FMRIB, Nuffield Dept. of Clinical Neurosciences, University of Oxford, UK

7 ^d Translational Imaging Group, Centre for Medical Image Computing, University College London, UK

8 A R T I C L E I N F O

9 Article history:

10 Received 24 September 2014

11 Accepted 30 June 2015

12 Available online xxx

13 Keywords:

14 Brain morphology

15 Lifespan brain aging

16 Dementia

17 Longitudinal analysis

18 Multi-level models

19 Bayesian inference

A B S T R A C T

We introduce a mass-univariate framework for the analysis of whole-brain structural trajectories using longitu- 20
dinal Voxel-Based Morphometry data and Bayesian inference. Our approach to developmental and aging 21
longitudinal studies characterizes heterogeneous structural growth/decline between and within groups. In 22
particular, we propose a probabilistic generative model that parameterizes individual and ensemble average 23
changes in brain structure using linear mixed-effects models of age and subject-specific covariates. Model inver- 24
sion uses Expectation Maximization (EM), while voxelwise (empirical) priors on the size of individual differences 25
are estimated from the data. Bayesian inference on individual and group trajectories is realized using Posterior 26
Probability Maps (PPM). In addition to parameter inference, the framework affords comparisons of models 27
with varying combinations of model order for fixed and random effects using model evidence. We validate the 28
model in simulations and real MRI data from the Alzheimer's Disease Neuroimaging Initiative (ADNI) project. 29
We further demonstrate how subject specific characteristics contribute to individual differences in longitudinal 30
volume changes in healthy subjects, Mild Cognitive Impairment (MCI), and Alzheimer's Disease (AD). 31

© 2015 Published by Elsevier Inc.

37 Introduction

38 Magnetic Resonance Imaging (MRI) and computational morphome- 52
try have become important tools for *in-vivo* analysis of changes in 53
healthy and pathological brain development and aging (Frononi et al., 54
2010; Fjell and Walhovd, 2010). One of the most exciting research ques- 55
tions is the nature of variability in aging brain structure (Raz et al., 2005, 56
2010; Raz and Rodrigue, 2006) and function (Pudas et al., 2013; Grady, 57
2012) observed across individuals. Most aging studies apply cross- 58
sectional designs, providing estimates of population average, age- 59
related, differences via pooling within cohorts (Ziegler et al., 2012a). 60
However, exploring the large heterogeneity of true within-subject 61
brain changes necessarily requires repeated measures and longitudinal 62
designs (Raz and Lindenberger, 2011). 63

64 Longitudinal assessments offer significant advantages over cross- 65
sectional studies (for an introduction see e.g. Fitzmaurice et al., 2008). 66

* Corresponding author at: Wellcome Trust Center for Neuroimaging, 12 Queen Square, 67
WC1N 3BG London, UK.

E-mail address: g.ziegler@ucl.ac.uk (G. Ziegler).

¹ Data used in preparation of this article were obtained from the Alzheimer's Disease 68
Neuroimaging Initiative (ADNI) database (www.loni.usc.edu/www.loni.usc.edu). As such, 69
the investigators within the ADNI contributed to the design and implementation of 70
ADNI and/or provided data but did not participate in analysis or writing of this report. A 71
complete listing of ADNI investigators can be found at [http://adni.loni.usc.edu/wp- 72
content/uploads/how_to_apply/ADNI_Acknowledgement_List.pdf](http://adni.loni.usc.edu/wp-content/uploads/how_to_apply/ADNI_Acknowledgement_List.pdf). 73

A longitudinal study is more powerful for a fixed number of subjects. 52
It permits separation of within- and between-subject variability, and 53
helps to ameliorate confounds. Another important advantage is that in 54
addition to providing estimates of population average brain changes it 55
enables a characterization of systematic differences in longitudinal tra- 56
jectories among individuals. This allows researchers to identify adverse 57
as well as protective factors that may influence healthy and pathological 58
changes in brain anatomy and function over time (see e.g. Taki et al., 59
2013; Thambisetty et al., 2012; Smith et al., 2010; Debette et al., 2011; 60
den Heijer et al., 2012). Moreover, individual subjects' trajectories are 61
promising biomarkers for early stage diagnosis (Chetelat and Baron, 62
2003), tracking of disease progression (Fonteiijn et al., 2012; Jedynak 63
et al., 2012; Sabuncu et al., 2014; Donohue et al., 2014; Young et al., 64
2014) and monitoring of potential treatments (Douaud et al., 2013). 65

Crucially, longitudinal MR-based morphometry is prone to artifacts 66
due to scanner inhomogeneities, registration inconsistency, and subtle 67
scanner-positioning or hydration-related deformations of the brains 68
(Schnaudigel et al., 2010; Littmann et al., 2006; Kempton et al., 2009). 69
Sophisticated within-subject registration pipelines have been intro- 70
duced recently to parameterize structural changes in an unbiased fash- 71
ion (Ashburner and Ridgway, 2013; Leung et al., 2012; Lorenzi and 72
Pennec, 2013; Holland et al., 2011; Reuter et al., 2010, 2012). 73

An essential difference between longitudinal and cross-sectional 74
analysis lies in the modeling assumptions about each individual. With 75
a single observation per subject one has to assume the process of 76

interest is identical across subjects (using fixed-effects assumptions). In contrast, longitudinal designs allow one to parameterize individual variations in the process by including random effects (or random coefficients). Modeling repeated measurements of behavior is well established in psychology and psychometry (for review see McArdle, 2009). In the last decade, there has been a growing interest in applications of mixed-effects models in the context of neuroimaging of development (Shaw et al., 2006, 2008; Raznahan et al., 2011a,b, 2014; Schumann et al., 2010) and aging neuroscience (Lerch et al., 2005; Lau et al., 2008; Carmichael et al., 2010). More articles focus specifically on methods for analysis of longitudinal MRI (Resnick et al., 2000; Chan et al., 2003; Frost et al., 2004; Bernal-Rusiel et al., 2012) and voxel-wise or vertex-wise longitudinal modeling (Guillaume et al., 2014; Li et al., 2013; Skup et al., 2012; Chen et al., 2013; Bernal-Rusiel et al., 2013).

Bayesian inference has been successfully applied to functional brain scans in multiple domains, ranging from general linear models, group analysis, spatial models, analysis of connectivity, to model comparisons (for extensive review see Woolrich, 2012). Bayesian inference typically exploits hierarchical observation models that take into account different levels of observations (e.g. scans and subjects), allows for the inclusion of biologically informed prior-beliefs about parameters, and affords comparisons among competing (nested or non-nested) models. Bayesian treatment of whole-brain neuroimaging data might also increase the sensitivity by finessing the problem of multiple comparison (Friston and Penny, 2003; Schwartzman et al., 2009). In contrast to classical inference, it also enables the assessment of evidence in favor of the null hypothesis; i.e., no aging-related change or preservation of structural integrity. These issues speak to a Bayesian framework for modeling structural change trajectories. However, there are currently only a few existing studies that consider longitudinal structural MRI (Schmid et al., 2009; Chen et al., 2012).

Here, we propose a generic modeling framework for longitudinal morphometric brain changes in development and aging studies. After diffeomorphic registration on the within-subject (Ashburner and Ridgway, 2013) and between-subject (Ashburner and Friston, 2011) level, we build a generative linear mixed-effects model of repeated observations. The model inversion flexibly accommodates unbalanced and sparse designs with potentially different numbers of follow up scans per subject. Using Expectation Maximization (EM) we obtain voxelwise individual and group level change parameters and compute Posterior Probability Maps (PPM) (Friston and Penny, 2003) for inference about regionally specific effects. In other words, we focus on making regionally specific inferences about longitudinal changes in anatomy, that properly account for both within and between subject variability in neurodevelopmental trajectories.

We validate the model using simulated data and a large MRI sample from the ADNI cohort. We then demonstrate a parametric analysis of subject specific covariates and explore the model space to optimize explanations of individual trajectory differences.

Methods

In this section, we introduce a generative model of local structural trajectories using random and fixed effects; i.e., a mixed effect, hierarchical or multilevel model. We describe the Bayesian formulation, the implicit (empirical) prior covariance components and their estimation using expectation maximization (EM). We extend this framework to modeling of trajectories over multiple groups and review the use of probabilistic parameter maps (PPM) for inference on model parameters. We conclude this section with a treatment of Bayesian model selection of ensemble trajectory models.

A generative model of local structural trajectories

The model for age-related changes of local brain structure (per voxel or region) is based upon the following generative model, which

comprises a likelihood and prior. The model is an application of the Bayesian linear hierarchical observation framework introduced by Friston et al. (2002a) (for application in the context of fMRI see also Friston et al., 2002b).

We here consider the special case of a two level model, one for individual structural trajectories and a second level for an ensemble of trajectories, denoted by ε . The first level likelihood model is based on the assumption that the trajectory of underlying volumetric changes is sampled from subject-specific functions of age or time

$$y_{ij} = g(t_{ij}, \theta_i^{(1)}) + \epsilon_{ij}^{(1)} \tag{1}$$

where the measurement y_{ij} is the j -th of m_i observations (e.g. of gray matter density at a single voxel) obtained from the i -th of N subjects at age t_{ij} , and $\epsilon_{ij}^{(1)}$ denotes an i.i.d. Gaussian measurement error with variance σ^2 . In what follows we use time centered t_{ij} in order to develop trajectories around the reference age, i.e. t_r , which typically is chosen as the mean age of the sample. Individual differences of trajectories are thus encoded by subject-specific change parameters $\theta_i^{(1)}$ resulting in an ensemble of age-related trajectories $\varepsilon = \{g(t, \theta_i^{(1)})\}_{i=1}^N$ for a sample of individuals. In particular, we parameterize the function describing the trajectory using a D degree polynomial expansion of age

$$g(t, \theta_i^{(1)}) = \sum_{d=1}^{D+1} \theta_{dt}^{(1)} t^{d-1} \tag{2}$$

with coefficients $\theta_i^{(1)} = [\theta_{1i}^{(1)}, \dots, \theta_{D+1i}^{(1)}]^T$. For example, for $D = 2$ we have 3 coefficients per subject, encoding the intercept, slope and quadratic terms. We can easily write these linear models using compact matrix notation with individual design matrices and change parameters as $\mathbf{g}_i = \mathbf{X}_i^{(1)} \theta_i^{(1)}$. Then, the model for all subjects follows

$$\begin{bmatrix} \mathbf{y}_1 \\ \mathbf{y}_2 \\ \vdots \\ \mathbf{y}_N \end{bmatrix} = \begin{bmatrix} \mathbf{X}_1^{(1)} & & & \\ & \mathbf{X}_2^{(1)} & & \\ & & \ddots & \\ & & & \mathbf{X}_N^{(1)} \end{bmatrix} \begin{bmatrix} \theta_1^{(1)} \\ \theta_2^{(1)} \\ \vdots \\ \theta_N^{(1)} \end{bmatrix} + \epsilon^{(1)} \tag{3}$$

$$\mathbf{y} = \mathbf{X}^{(1)} \boldsymbol{\theta}^{(1)} + \epsilon^{(1)} \tag{4}$$

with subject i -th observations $\mathbf{y}_i = [y_{i1}, y_{i2}, \dots, y_{im_i}]^T$, $M = \sum m_i$ concatenated observations \mathbf{y} , first level design matrix $\mathbf{X}^{(1)}$, concatenated change parameters $\boldsymbol{\theta}^{(1)}$, and first level Gaussian errors $\epsilon^{(1)}$. Vectorizing observations y_{ij} in ‘person-scan’ format, i.e. the successive scans are grouped by subjects (all from subject 1, all from subject 2, etc.), is a natural way to arrange longitudinal data with missing scans and varying number of follow ups. This additionally simplifies the structure of the first level design matrix, which then takes a block-diagonal form. Note, that this first level model explicitly accommodates unbalanced designs, i.e. $\mathbf{X}_i^{(1)} \neq \mathbf{X}_j^{(1)}$, with varying ages and numbers of scans per subject.

The sample change parameters of the trajectory functions are determined by (primarily non-age-dependent) subject specific effects. Note that these second level regressors can be chosen to model covariates of interest, e.g. IQ scores, genetic markers, or symptom severity, as well as purely confounding variables, e.g. global brain parameters. These measures are summarized in a centered $N \times R$ between-subject covariates matrix \mathbf{Z} with entries z_{ir} . For example, in the results section below, we use a genetic risk score as a covariate of interest and test to see how this predicts first level parameters. Now, we adopt the following linear second level model

$$\begin{bmatrix} \theta_1^{(1)} \\ \theta_2^{(1)} \\ \vdots \\ \theta_N^{(1)} \end{bmatrix} = \begin{bmatrix} \mathbf{I} & z_{11}\mathbf{I} & & z_{1R}\mathbf{I} \\ & \mathbf{I} & & z_{2R}\mathbf{I} \\ & & \ddots & \vdots \\ & & & \mathbf{I} & z_{N1}\mathbf{I} & & z_{NR}\mathbf{I} \end{bmatrix} \begin{bmatrix} \theta_1^{(2)} \\ \theta_2^{(2)} \\ \vdots \\ \theta_{R+1}^{(2)} \end{bmatrix} + \epsilon^{(2)} \tag{5}$$

189 $\boldsymbol{\theta}^{(1)} = \mathbf{X}^{(2)}\boldsymbol{\theta}^{(2)} + \boldsymbol{\epsilon}^{(2)}$ (6)

191 with $D + 1$ dimensional identity matrix \mathbf{I} , second level design matrix $\mathbf{X}^{(2)}$, concatenated parameters $\boldsymbol{\theta}^{(2)}$, and zero mean multivariate Gaussian errors $\boldsymbol{\epsilon}^{(2)}$ respectively (for distributions details see also **Q3** [Covariance component specification](#) section). Note, that we can further simplify the structure of the design matrix by writing it as a Kronecker product $[[\mathbf{1}_N \mathbf{Z}] \otimes \mathbf{I}_{D+1}]$ using N dimensional column vector of ones $\mathbf{1}_N$. Although one could choose a separate set of covariates for each trajectory parameter, we here consider the common exploratory situation where one is interested in potential effects of a small set of covariates on all trajectory properties, i.e. intercept, slope, etc.

200 Due to the particular choice of a column of ones in the second level design, it follows that $\boldsymbol{\theta}^{(2)}$ parameterizes the sample average change in terms of a mean trajectory, which is the expectation for every subject's trajectory parameters after accounting for covariate effects. The remaining second level parameters $\boldsymbol{\theta}_2^{(2)}, \dots, \boldsymbol{\theta}_{R+1}^{(2)}$ become the coefficients of each covariate's contribution to individual trajectory differences.

207 *Combining fixed and random effects*

208 The above model with degree zero might be referred to as the random intercept model without slope. Using this model in the context of longitudinal MRI assumes variability of structure across subjects but no changes over time. If we chose model degree one, the model now includes a random slope parameter for every subject. One might argue that the first (or higher) degree(s) can also enter as fixed (as opposed to random effects); e.g., assuming the same rate of change (or quadratic effect) for all subjects. The above framework naturally extends to modeling these additional fixed effects of degree d by appending column vectors \mathbf{x}_f^d with entries $t_{im_i}^d$ to the first level design matrix $[\mathbf{X}^{(1)}, \mathbf{x}_f^{D+1}, \dots, \mathbf{x}_f^{D_f}]$. In this case we need to extend first level parameters accordingly, i.e. $\boldsymbol{\theta}^{(1)} = [\boldsymbol{\theta}_1^{(1)}, \dots, \boldsymbol{\theta}_N^{(1)}, \boldsymbol{\theta}_f^{(1)}]$. In presence of these fixed effects the second level design follows as

222
$$\begin{bmatrix} \boldsymbol{\theta}^{(1)} \\ \boldsymbol{\theta}_f^{(1)} \end{bmatrix} = \begin{bmatrix} \mathbf{X}^{(1)} & \mathbf{0} \\ \mathbf{0} & \mathbf{I}_{D_f-D} \end{bmatrix} \begin{bmatrix} \boldsymbol{\theta}^{(2)} \\ \boldsymbol{\theta}_f^{(2)} \end{bmatrix} + \begin{bmatrix} \boldsymbol{\epsilon}^{(2)} \\ \boldsymbol{\epsilon}_f^{(2)} \end{bmatrix}. \quad (7)$$

223 If we now constrain the second level errors for fixed effects parameters to be zero, we can perform second level group inference for random and fixed effects parameters in a similar way (as will be shown in the [Bayesian perspective](#) section). In what follows we use D to denote the degree of random effects and D_f for the degree of fixed effects. Please note that entering fixed effects, in addition to random effects of the same degree, would result in redundant parameters for the average trajectory. Thus, one might prefer only using additional fixed effects with higher degrees $D_f > D$. This parametrization of fixed and random effects is motivated by our hierarchical formulation of the model and might slightly differ from standard mixed-effects textbooks.

233 *Covariance component specification*

234 In order to estimate the above model, we need to fully specify all covariance constraints for first and second level errors, further denoted with $\mathbf{C}_\epsilon^{(1)}$ and $\mathbf{C}_\epsilon^{(2)}$ respectively. Given an unknown covariance structure \mathbf{C} we use a small set of covariance basis functions \mathbf{Q}_k and estimate the corresponding coefficients or hyperparameters λ_k

240
$$\mathbf{C}(\boldsymbol{\lambda}) = \sum_k \lambda_k \mathbf{Q}_k. \quad (8)$$

241 More generally, this can be motivated by a first-order Taylor expansion of the covariances with respect to their hyperparameters (for details see e.g. [Friston et al., 2002a](#)). This idea will be now outlined for all

243 covariance components of the above model. We begin with a single group design, and extend this to modeling of multiple groups in later sections. It is important to note that the covariance could be specified being linear in the hyperparameters (as seen in Eq. (8)); however, this does not preclude negative definite covariances ([Harville, 1977](#)). In contrast to optimizing linear coefficients λ , in what follows, we optimize log-covariance parameters, i.e. e^λ . This forces the hyperparameters to be positive and at the same time increases the stability of the subsequent optimization scheme.

252 In particular, as mentioned above, we specify the first level error covariance using an isotropic noise model

253
$$\mathbf{C}_\epsilon^{(1)} = e^{\log(\sigma^2)} \mathbf{I}_M \quad (9)$$

255 with \mathbf{I}_M denoting an identity matrix and noise variance σ^2 . This models unstructured errors of measurement, e.g. due to MRI noise and random errors or minor inaccuracies during preprocessing. Furthermore we recall that every subject is fully described by its parameter vector $\boldsymbol{\theta}_i^{(1)}$. Considering the population, however, there is unknown variability of individual parameters across subjects, which is either explicitly modeled by covariates (or group structures) in design matrix $\mathbf{X}^{(2)}$ or captured by the second level error covariance $\mathbf{C}_\epsilon^{(2)}$. The unexplained individual differences might differentially affect all trajectory coefficients and thus (at least) one further hyperparameter for each of the trajectory parameters is required. We therefore use λ_1, λ_2 , etc. to describe unexplained individual differences of intercept, slope etc. For that purpose we use \mathbf{R}_i to denote the covariance matrix of residual parameter vectors $\text{Cov}(\boldsymbol{\epsilon}_i)$ and we suppose

267
$$\mathbf{R}_i = \begin{bmatrix} e^{\lambda_1} & & \\ & \ddots & \\ & & e^{\lambda_{D+1}} \end{bmatrix}. \quad (10)$$

269 Typically, having only very sparse observations in longitudinal MRI designs prevents us from estimating \mathbf{R}_i on the individual level. For reasons of identifiability in a wide range of designs, we therefore assume the same residual covariance across all subjects, i.e. $\mathbf{R}_i = \mathbf{R}$. The full second level error covariance can be therefore specified as follows

274
$$\mathbf{C}_\epsilon^{(2)} = \begin{bmatrix} \mathbf{R} & & \\ & \ddots & \\ & & \mathbf{R} \end{bmatrix} = \mathbf{I}_N \otimes \mathbf{R} = \sum_{d=1}^{D+1} e^{\lambda_d} \mathbf{Q}_d \quad (11)$$

276 where covariance basis functions \mathbf{Q}_d can be efficiently implemented exploiting the Kronecker product. Taken together $[\sigma^2, \lambda_1, \dots, \lambda_{D+1}]$ fully parameterize the covariance components of the model in its simplest form; resulting, e.g. in three voxelwise hyperparameters for single ensembles of linear trajectories. Please note that the above framework nicely extends to more complex models, e.g. with first level covariates and correlated residuals at the second level.

281 Finally, we finesse the covariance components to account for any fixed effects as discussed in the [Combining fixed and random effects](#) section. This means we consider the case when the degree of fixed effects exceeds the degree of random effects and we apply extended design matrices and parameters (Eq. (7)). In order to perform similar inference for second level fixed effects parameters like group average parameters of random effects we enforce identity of first and second level fixed effects parameters, i.e. $\boldsymbol{\theta}_f^{(1)} = \boldsymbol{\theta}_f^{(2)}$. This can be easily implemented by choosing a hyperparameter of second level fixed effects errors with a very small variance, i.e. $\boldsymbol{\epsilon}_f^{(2)} \sim \mathcal{N}(\mathbf{0}, \sigma_f^2 \mathbf{I}_{D_f-D})$ with e.g. $\sigma_f^2 = e^{-32}$.

293 Bayesian perspective

294 We now explore the Bayesian perspective on the above model for an
 295 ensemble of trajectories (defined by Eqs. (4) and (6)). A key aspect of
 296 this formulation is that we can consider the second level to furnish an
 297 empirical prior for the first level parameters, as follows

299
$$P(\mathbf{y}|\boldsymbol{\theta}^{(1)}) = \mathcal{N}(\mathbf{y}; \mathbf{X}^{(1)}\boldsymbol{\theta}^{(1)}, \mathbf{C}_\epsilon^{(1)}) \quad (12)$$

300
$$P(\boldsymbol{\theta}^{(1)}|\boldsymbol{\theta}^{(2)}) = \mathcal{N}(\boldsymbol{\theta}^{(1)}; \mathbf{X}^{(2)}\boldsymbol{\theta}^{(2)}, \mathbf{C}_\epsilon^{(2)}) \quad (13)$$

302 with error covariances $\mathbf{C}_\epsilon^{(k)}$, $k = 1, 2$. The first level error covariance cor-
 303 responds to measurement noise.

304 Finally, we assume second level priors on the ensemble change param-
 305 eters. At the end of this section we will briefly discuss promising
 choices of priors which might be relevant for potential applications:

307
$$P(\boldsymbol{\theta}^{(2)}) = \mathcal{N}(\boldsymbol{\theta}^{(2)}; \boldsymbol{\eta}_\theta^{(2)}, \mathbf{C}_\theta^{(2)}) \quad (14)$$

308 The hierarchical structure of the trajectory model implies that the
 joint probability factorizes as

310
$$P(\mathbf{y}, \boldsymbol{\theta}^{(1)}, \boldsymbol{\theta}^{(2)}) = P(\mathbf{y}|\boldsymbol{\theta}^{(1)})P(\boldsymbol{\theta}^{(1)}|\boldsymbol{\theta}^{(2)})P(\boldsymbol{\theta}^{(2)}) \quad (15)$$

311 rendering the data conditionally independent of the second level param-
 312 eters given the first level parameters (Bishop, 2006).

313 In this framework, hierarchical model inversion corresponds to esti-
 314 mating covariance components $\mathbf{C}_\epsilon^{(1)}$, $\mathbf{C}_\epsilon^{(2)}$ and $\mathbf{C}_\theta^{(2)}$ respectively. For this
 purpose, the model can be further rearranged in a non-hierarchical
 form (see also Friston et al., 2002a)

316
$$\mathbf{y} = [\mathbf{X}^{(1)} \quad \mathbf{X}^{(1)}\mathbf{X}^{(2)}] \begin{bmatrix} \boldsymbol{\epsilon}^{(2)} \\ \boldsymbol{\theta}^{(2)} \end{bmatrix} + \boldsymbol{\epsilon}^{(1)}. \quad (16)$$

317 Exploiting the Bayesian perspective, we treat the second level errors
 318 as additional model parameters, which will be estimated in subsequent
 319 steps.

320 To ensure all covariance components are evaluated simultaneously,
 321 we further augment the model by adding rows that correspond to the
 prior expectation $E[\boldsymbol{\epsilon}^{(2)}] = 0$ and $E[\boldsymbol{\theta}^{(2)}] = \boldsymbol{\eta}_\theta^{(2)}$ respectively

323
$$\begin{bmatrix} \mathbf{y} \\ \mathbf{0} \\ \boldsymbol{\eta}_\theta^{(2)} \end{bmatrix} = \begin{bmatrix} \mathbf{X}^{(1)} & \mathbf{X}^{(1)}\mathbf{X}^{(2)} \\ \mathbf{I} & \mathbf{0} \\ \mathbf{0} & \mathbf{I} \end{bmatrix} \begin{bmatrix} \boldsymbol{\epsilon}^{(2)} \\ \boldsymbol{\theta}^{(2)} \end{bmatrix} + \begin{bmatrix} \boldsymbol{\epsilon}^{(1)} \\ -\boldsymbol{\epsilon}^{(2)} \\ \boldsymbol{\eta}_\theta^{(2)} - \boldsymbol{\theta}^{(2)} \end{bmatrix} \quad (17)$$

324
$$\bar{\mathbf{y}} = \bar{\mathbf{X}}\boldsymbol{\theta} + \bar{\boldsymbol{\epsilon}} \quad (18)$$

326 with augmented data $\bar{\mathbf{y}}$, augmented design $\bar{\mathbf{X}}$ and parameters $\boldsymbol{\theta}$ and aug-
 327 mented errors $\bar{\boldsymbol{\epsilon}}$. Note that in contrast to the models considered above
 328 the augmented error contains all covariance components of the two-
 329 level model. One further benefit of augmentation is that it allows formulat-
 330 ing the Gaussian likelihood and prior of the ensemble trajectories in a
 pleasingly compact form

332
$$p(\bar{\mathbf{y}}|\boldsymbol{\theta}) = \mathcal{N}(\bar{\mathbf{y}}; \bar{\mathbf{X}}\boldsymbol{\theta}, \mathbf{C}_\epsilon) \quad (19)$$

333
$$p(\boldsymbol{\theta}) = \mathcal{N}(\boldsymbol{\theta}; \boldsymbol{\eta}_\theta, \mathbf{C}_\theta) \quad (20)$$

335 with expectation and covariance components

336
$$\boldsymbol{\eta}_\theta = \begin{bmatrix} 0 \\ \boldsymbol{\eta}_\theta^{(2)} \end{bmatrix}, \mathbf{C}_\epsilon = \begin{bmatrix} \mathbf{C}_\epsilon^{(1)} & 0 \\ 0 & \mathbf{C}_\epsilon^{(2)} \end{bmatrix}, \mathbf{C}_\theta = \begin{bmatrix} \mathbf{C}_\theta^{(2)} & 0 \\ 0 & \mathbf{C}_\theta^{(2)} \end{bmatrix}. \quad (21)$$

337 Longitudinal MRI studies of healthy and pathological development
 rest on inferences about first or second level parameters of the above

model. The posterior density over parameters, given a particular sample
 of observations, is also Gaussian and can be written using the compact
 Gauss–Markov form

342
$$P(\boldsymbol{\theta}|\mathbf{y}) = \mathcal{N}(\boldsymbol{\theta}; \boldsymbol{\eta}_{\theta|\mathbf{y}}, \mathbf{C}_{\theta|\mathbf{y}}) \quad (22)$$

343
$$\mathbf{C}_{\theta|\mathbf{y}} = (\bar{\mathbf{X}}^T \mathbf{C}_\epsilon^{-1} \bar{\mathbf{X}})^{-1} \quad \text{and} \quad (23)$$

344
$$\boldsymbol{\eta}_{\theta|\mathbf{y}} = \mathbf{C}_{\theta|\mathbf{y}} (\bar{\mathbf{X}}^T \mathbf{C}_\epsilon^{-1} \mathbf{y}). \quad (24)$$

345 The ensuing model inversion can be performed in a fully Bayesian
 346 way, i.e. using an informative prior on top level parameters; i.e., with
 347 given $\boldsymbol{\eta}_\theta^{(2)}$ and $\mathbf{C}_\theta^{(2)}$. These prior distributions can be specified based on
 348 expectations from the literature or as suggested in Friston and Penny
 349 (2003) one might apply empirically derived prior distributions using
 350 the data at hand, e.g. obtained from a pooled covariance estimate. More-
 351 over, if one does not have explicit prior assumptions about the local pat-
 352 terns of change, one can treat these parameters as unknown, thus using
 353 uninformative priors.

354 In this particular study we apply uninformative or flat priors with
 355 $\mathbf{C}_\theta^{(2)} = \infty$ (or equivalently $(\mathbf{C}_\theta^{(2)})^{-1} = 0$), with the prior expectation
 356 $\boldsymbol{\eta}_\theta^{(2)}$ set to zero. In order to obtain the posterior over all trajectory pa-
 357 rameters, we estimate the covariance components using an EM scheme.
 358 As described above, the top level prior covariance is unknown, realized
 359 by setting it to an arbitrarily high value, in particular we choose $\mathbf{C}_\theta^{(2)} =$
 360 $e^{32}\mathbf{I}$. A simple illustration of the applied model is shown in Fig. 1.

364 Model estimation using Expectation Maximization (EM)

365 As proposed by Friston et al. (2002a) we adapt an Expectation Max-
 366 imization (EM) algorithm (Dempster et al., 1977) to obtain all covari-
 367 ance components and the posterior of the change parameters. EM
 368 iteratively refines a lower bound F on the log-likelihood of the data
 369 given the hyperparameters, i.e. $\ln p(\mathbf{y}|\boldsymbol{\lambda}) \geq F(q(\boldsymbol{\theta}), \boldsymbol{\lambda})$, where $q(\boldsymbol{\theta})$
 370 is any distribution of the change parameters. Using iterative alternation
 371 between E and M steps (see later), one performs a coordinate ascent
 372 on F , and thus implicitly increases the log-likelihood.

373 E-Step

374 Under the above Gaussian assumptions, each E-step maximizes
 375 $F(q(\boldsymbol{\theta}), \boldsymbol{\lambda})$ with respect to the distribution $q(\boldsymbol{\theta})$. Here, this simply corre-
 376 sponds to obtaining sufficient statistics for the posterior of the param-
 377 eters, i.e. F is maximized by $q(\boldsymbol{\theta}) = p(\boldsymbol{\theta}|\mathbf{y}, \boldsymbol{\lambda})$. Using the covariance

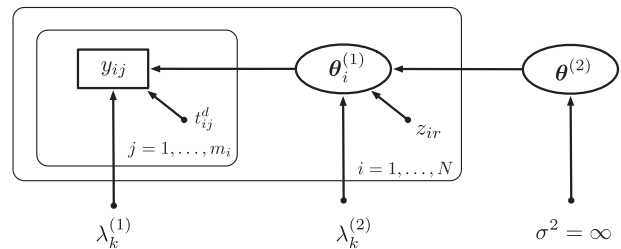


Fig. 1. Illustration of the trajectory model using a directed graphical model emphasizing the Bayesian perspective. Rectangles are used for observed variables, e.g. y_{ij} is the j -th observation of the i -th subject. Ellipsoids are used for latent (or hidden) stochastic variables, e.g. $\theta_i^{(1)}$ refers to intercept, slope, etc. of the i -th subject. $\theta^{(2)}$ denotes all second level parameters, e.g. all group's average intercept, slope, and covariate effects. All other parameters with arrows denote deterministic variables, e.g. z_{ir} is the r -th covariate for the i -th subject or the timepoint t_{ij} of the j -th observation of the i -th subject. For the top level parameters, we apply flat priors denoted by an infinite prior variance parameter. We have introduced plates that compactly represent multiple variables (and arrows), for which only a single example is shown explicitly.

378 parametrization of the augmented model and Eqs. (23) and (24) the
379 posterior is given by

$$381 \boldsymbol{\eta}_{\theta|y} = \mathbf{C}_{\theta|y} \bar{\mathbf{X}}^T \mathbf{C}_\epsilon^{-1} \bar{y} \quad (25)$$

$$382 \mathbf{C}_{\theta|y} = \left(\bar{\mathbf{X}}^T \mathbf{C}_\epsilon^{-1} \bar{\mathbf{X}} \right)^{-1} \text{ and} \quad (26)$$

$$384 \mathbf{C}_\epsilon = \mathbf{C}_\theta + \sum_k e^{\lambda_k} \mathbf{Q}_k. \quad (27)$$

387

M-Step

388 Here, we optimize $F(q(\boldsymbol{\theta}), \boldsymbol{\lambda})$ with respect to the covariance
389 hyperparameters, in a maximum likelihood sense, using the posterior
390 distribution obtained during the preceding E-step. In particular, F during
391 the M-step is given by

$$F = \frac{1}{2} \ln |\mathbf{C}_\epsilon^{-1}| - \frac{1}{2} \mathbf{r}^T \mathbf{C}_\epsilon^{-1} \mathbf{r} - \frac{1}{2} \text{tr} \left(\mathbf{C}_{\theta|y} \bar{\mathbf{X}} \mathbf{C}_\epsilon^{-1} \bar{\mathbf{X}} \right) + \frac{1}{2} \ln |\mathbf{C}_{\theta|y}| + \text{const} \quad (28)$$

393 with residuals $\mathbf{r} = \bar{y} - \bar{\mathbf{X}} \boldsymbol{\eta}_{\theta|y}$ (for an exact derivation see Friston et al.,
2002a). The first term decreases F with a larger number and size of
394 hyperparameters, while the second term increases F with smaller precision
395 weighted residuals corresponding to a better model fit.

396 Note also, that during the M-step the posterior covariance $\mathbf{C}_{\theta|y}$ is a
397 fixed result from the preceding E-step, while $\mathbf{C}_\epsilon = \mathbf{C}_\epsilon(\boldsymbol{\lambda})$ depends on
398 the hyperparameters and will be optimized. Thus in general the
399 third term of F is not the trace of an identity matrix. The last term,
400 which stems from the entropy of the distribution over change parameters
401 $q(\boldsymbol{\theta})$, can be neglected, because it does not depend on the
402 hyperparameters.

403 To update the hyper parameters we adopt a Fisher scoring algo-
404 rithm, using the first derivative (or gradient) \mathbf{g} and the expected second
405 partial derivatives (or Fisher's Information matrix) \mathbf{H} :

$$407 \boldsymbol{\lambda} = \boldsymbol{\lambda} + \mathbf{H}^{-1} \mathbf{g} \text{ with} \quad (29)$$

$$408 \mathbf{g}_k = \frac{\partial F}{\partial \lambda_k} = -\frac{1}{2} e^{\lambda_k} \left(\text{tr}(\mathbf{P} \mathbf{Q}_k) - \bar{y}^T \mathbf{P}^T \mathbf{Q}_k \mathbf{P} \bar{y} \right), \quad (30)$$

$$410 H_{kl} = \mathbb{E} \left[\frac{\partial^2 F}{\partial \lambda_k \partial \lambda_l} \right] = \frac{1}{2} e^{\lambda_k + \lambda_l} \text{tr}(\mathbf{P} \mathbf{Q}_k \mathbf{P} \mathbf{Q}_l), \text{ and} \quad (31)$$

$$413 \mathbf{P} = \mathbf{C}_\epsilon^{-1} - \mathbf{C}_\epsilon^{-1} \bar{\mathbf{X}} \mathbf{C}_{\theta|y} \bar{\mathbf{X}}^T \mathbf{C}_\epsilon^{-1}. \quad (32)$$

416 The updated hyperparameters re-enter into the estimation of the
417 posterior in the next E-step.² Finally, after appropriate initialization of
418 the hyperparameters $\boldsymbol{\lambda}$, the full algorithm alternates between the E-
419 and M-steps until convergence.

Multiple groups

420 Longitudinal studies of development and aging often aim at infer-
421 ence about differences among average population trajectories. Typic-
422 ally, this involves comparing change rates (or slope differences) in
423 healthy vs. pathological development, specific treatment conditions, or
424 groups following specific lifestyle patterns. Although the ongoing struc-
425 tural change is well characterized by the slope parameters, the current
426 framework also supports inference about other aspects of trajectory
427 shape; e.g., intercepts or higher order non-linearities.

² Please note that the actual implementation uses $\Delta \boldsymbol{\lambda} = \bar{\mathbf{H}}^{-1} \mathbf{g}$ with $\bar{H}_{kl} = H_{kl} - P_h$ and hyperpriors $P_h = 1/32$. The treatment of hyperparameters using a probabilistic perspective is motivated within the variational Bayes framework (Friston et al., 2007) and increases numerical stability of the optimization scheme.

We therefore generalize the above model to situations where one
429 observes M scans of $N = N_1 + N_2 + \dots + N_G$ subjects, who are individ-
430 uals from G different populations with (mainly non-age dependent)
431 subject-specific covariates $\mathbf{Z}_1, \dots, \mathbf{Z}_G$. For example, we might consider
432 three groups of subjects in the ADNI dataset, including controls, MCI
433 and AD, with Mini Mental State Examination scores as covariates. The
434 subsamples are further used to estimate independent ensembles of tra-
435 jectories $\epsilon_1, \dots, \epsilon_G$ using the same trajectory parametrization (Eq. (4)),
436 e.g. quadratic curves. The assumptions about the group structure of tra-
437 jectories can be realized by modifying the second level design matrix (in
438 Eq. (6)) appropriately
439

$$\mathbf{X}^{(2)} = \begin{bmatrix} \mathbf{1}_{N_1} \mathbf{Z}_1 & & & \\ & \mathbf{1}_{N_2} \mathbf{Z}_2 & & \\ & & \ddots & \\ & & & \mathbf{1}_{N_G} \mathbf{Z}_G \end{bmatrix} \otimes \mathbf{I}_{D+1}. \quad (33)$$

In addition to allowing for different average trajectories in
442 different groups, the amount of individual differences within each
443 ensemble ϵ_g might also differ across populations. This is easily
444 achieved by adapting the model of the second level covariance
445 components to include independent hyperparameters for each
446 group.

We suppose the covariance structure of second level residuals to be
447 $\text{Cov}(\epsilon_i^{(2)}) = \mathbf{R}_g$ for subject i from group g . We again exploit diagonal co-
448 variance basis functions \mathbf{Q}_d (see Covariance component specification
449 section) to parameterize the variability of all change parameters in all
450 groups resulting in $G(D + 1)$ hyperparameters for the second level
451 model
452

$$\mathbf{C}_\epsilon^{(2)} = \begin{bmatrix} \mathbf{I}_{N_1} \otimes \mathbf{R}_1 & & & \\ & \mathbf{I}_{N_2} \otimes \mathbf{R}_2 & & \\ & & \ddots & \\ & & & \mathbf{I}_{N_G} \otimes \mathbf{R}_G \end{bmatrix} = \sum_{d=1}^{G(D+1)} e^{\lambda_d} \mathbf{Q}_d. \quad (34)$$

Note that one could include fixed effects of time or age. In many
454 practical applications these would enter as group specific fixed ef-
455 fects for each group and trajectory parameter. Finally, having speci-
456 fied a single or multi-group trajectory model, the estimation of
457 parameters and covariance components proceeds using EM as
458 described above.
459

Inference about group differences and analysis of individual differences of change

To facilitate practical applications to longitudinal MRI studies, we
462 also need to consider Bayesian inference about population differences
463 and subject specific covariate effects on individual trajectories. These ef-
464 fects can be characterized using the usual approach of defining contrasts
465 for linear models as commonly used in Statistical Parametric Mapping
466 (SPM) (Friston et al., 1995). In particular, single contrast vectors are
467 used to specify a single hypothesis about first or second level change pa-
468 rameters. For example, let us suppose a design with linear trajectories
469 (first level) and two groups and no covariates (second level). If we use
470 contrast vector $\mathbf{c} = [0, 1, 0, -1]^T$, then $\mathbf{c}^T \boldsymbol{\theta}^{(2)} = 0$ tests the (null) hy-
471 pothesis that the rate of change (slope) in group one is equal to the
472 slope in group two. Moreover, multiple contrast vectors can be used to
473 specify compound hypotheses. If $\mathbf{c}_1 = [1, 0, -1, 0]^T$, and $\mathbf{c}_2 =$
474 $[0, 1, 0, -1]^T$ then $[\mathbf{c}_1, \mathbf{c}_2]^T \boldsymbol{\theta}^{(2)} = \mathbf{0}$ assumes both intercepts and slopes
475 to be same across groups.
476

Posterior Probability Maps (PPM) were introduced for Bayesian infer-
477 ence on mass-univariate general linear models used in neuroimaging
478 (Friston and Penny, 2003). When applying PPMs, one is often interested
479 in the probability of linear contrasts $c = \mathbf{c}^T \boldsymbol{\theta}^{(2)}$ exceeding a certain
480 threshold, e.g. $\gamma = 0$. One can additionally specify a nonzero probability
481 threshold, typically $p_t = 0.95$. We are now in a position to construct
482

483 PPMs for Bayesian inference on arbitrary trajectory parameter contrasts
484 by voxelwise evaluation of the posterior

$$p(c > \gamma | \mathbf{y}) = 1 - \Phi \left(\frac{\gamma - \mathbf{c}^T \boldsymbol{\eta}_{\theta | \mathbf{y}}}{\sqrt{\mathbf{c}^T \mathbf{C}_{\theta | \mathbf{y}} \mathbf{c}}} \right) > p_t \quad (35)$$

486 with the cumulative density function of the unit normal distribution Φ .
487 Similarly, this framework affords comparison of structural change of
single individuals using the first level individual change parameters $\boldsymbol{\theta}^{(1)}$.

488 Comparison of different trajectory models

489 The above framework for individual trajectory estimation requires
490 an *a-priori* assumption about the polynomial order of random or fixed
491 effects. Generally, comparing various trajectory models corresponds to
492 the evaluation of competing hypotheses about trajectories in develop-
493 ment, aging and pathology or about nonlinear changes during the
494 lifespan. One can also use model comparison to test for differences
495 among groups, e.g. H0: all subjects in same group vs. H1: subjects in
496 control, MCI and AD groups. Crucially, one can use Bayesian model com-
497 parison to optimize aspects of the models about which ones uncertain
498 such as the degree order of the polynomial is above. Practically, Baye-
499 sian model comparison rests upon model evidence that is approximated
500 by the free energy obtained from EM. This (lower bound) approxima-
501 tion to log model evidence is used to monitor convergence during param-
502 eter estimation of any particular model and optimize the model
503 per se.

504 Bayesian model comparison has been suggested as a principled ap-
505 proach for inference about nested and non-nested models of neuroim-
506 aging data (Penny et al., 2004; Penny, 2012). Assuming the same prior
507 probability for both model orders, different orders can be compared
508 using the difference in free energy or log evidence. This corresponds
509 to the log Bayes factor (Kass and Raftery, 1995). Local voxelwise eval-
510 uation of this probability ratio compares model evidences of models with
511 different degrees

$$\text{BF} = \frac{P(\mathbf{y} | D = i)}{P(\mathbf{y} | D = j)} \quad (36)$$

513 or models with and without some additional fixed effects. Observing
514 $\text{BF} > 1$ in the above example indicates that it is more likely that individ-
515 ual differences of change are better captured by order i compared to j .

516 Questions about model order can be addressed flexibly using nested
517 model comparisons. Two models are nested when the smaller (e.g. lin-
518 ear) model is obtained by setting some parameters of the larger (e.g.
519 quadratic) model to zero. Note however, that this comparison of
520 model evidence naturally extends to non-nested models, e.g. comparing
two models with two different sets of covariates.

521 Summary of methods

522 In summary, we propose a hierarchical generative model to infer
523 families of (nonlinear) trajectories reported by longitudinal changes in
524 local brain volumes (or tissue densities). The key aspect of this model
525 is its hierarchical structure, wherein the first (within-subject) level ac-
526 commodates longitudinal effects whose trajectory depends upon
527 group average parameters at the second (between-subject) level. Cruci-
528 ally, this level includes differences in subjects that may be of interest;
529 for example, group differences or diagnosis, behavior or genetic vari-
530 ables (see later). Alternatively, second level effects may be considered
531 as confounds; for example, the age of a subject (e.g., at baseline), their
532 gender, or brain/head size (Barnes et al., 2010). By modeling nonlinear
533 trajectories in this fashion, one can easily accommodate unbalanced
534 designs, while exploiting the efficiency of mixed-effects inference and
535 associated parameter estimates.

Results

Validation using simulated structural trajectories

538 In what follows, we address the face validity of the above approach
539 using simulated data generated by the model with linear trajectories
540 drawn from the range of design and (hyper-) parameter specifications
541 typical of longitudinal MRI and VBM preprocessing. The simulated
542 data were entered into EM to compare parameter estimates with the
543 ground truth. This basically establishes the model inversion can recover
544 veridical parameter estimates. This validation procedure followed two
545 steps.

546 Firstly, simulation of an ensemble of trajectories corresponding to a
547 set of parameters $\boldsymbol{\theta}^{(1)}$ with specified average and individual trajectory
548 differences. In the above generative model, this corresponds to the
549 case of having only a column of ones in the second level design. Second
550 level average change parameters were fixed to $\boldsymbol{\theta}^{(2)} = [1.2, -5 \cdot 10^{-3}]^T$,
551 i.e. the mean intercept is 1.2 and mean slope is $-5 \cdot 10^{-3}$. No subject
552 covariates were included in these simulations. To evaluate model per-
553 formance in different contexts, the individual differences of the inter-
554 cept and the slope, i.e. $[\lambda_1, \lambda_2]$, were either assumed to be large
555 $[10^{-2}, 10^{-4}]$ or small $[10^{-4}, 10^{-6}]$ respectively. Illustrations of simulat-
556 ed trajectories are shown in Fig. 2A.

557 Secondly, performing longitudinal MRI acquisition is equivalent to
558 sparse temporal sampling of the unknown ground truth trajectories.
559 The sampling process is specified by the first level design matrix. How-
560 ever, longitudinal MRI studies might vary substantially with respect to
561 two main design characteristics. Designs can be more or less balanced
562 with respect to age and differ with respect to the number of follow up
563 measures per subject, i.e. more or less sparse. The simulation of MRI
564 sampling and other design factors are illustrated in Fig. 2B.

565 Fig. 3 shows the root mean squared error of the first and second level
566 intercept and slope parameters comparing the ground truth and the
567 model estimations.

568 In general the change parameter estimates obtained from EM were
569 found to be highly accurate, supporting the validity of the proposed
570 method for different designs. As expected for a hierarchical model, the
571 second level (group) parameter estimates were generally closer to the
572 ground truth than first level (individual) change parameters. In our sim-
573 ulations, higher noise levels (or first level errors) primarily impaired
574 first level parameter estimation accuracy.

575 To a minor extent, the first level noise also significantly affected the
576 second level slope estimates, especially in sparse balanced designs. Sim-
577 ilarly, larger individual differences (or second level errors) were found
578 to increase estimation errors of the second level. Interestingly, larger in-
579 dividual differences also resulted in increased first level parameter er-
580 rors, especially for less balanced designs.

581 We further found that having fewer follow up scans (or higher spar-
582 sity) in longitudinal designs broadly compromises individual and group
583 level parameter estimates. Sparsity particularly affected all first level pa-
584 rameters in balanced and less balanced designs and the second level
585 slope estimates; especially in balanced designs with more observational
586 noise. In contrast, using more or less balanced designs had differential
587 effects on estimation accuracy. Trajectory intercept errors were in-
588 creased by more balanced designs, while slope estimates seemed at
589 least in part to be improved.

590 As our model is based on assumptions about Gaussian distributions,
591 the model inversion and inference might be affected by any violation of
592 this assumption. A second row of simulations was conducted to test the
593 validity of our model inversion in the presence of non-Gaussian error
594 distributions (Fig. 4). We explicitly manipulated skewness and kurtosis
595 of the first and second level errors and assessed the stability and accu-
596 racy of group trajectory rate of change (slope) and the corresponding var-
597 iability hyperparameter, i.e. λ_2 . Interestingly, we observed that rates of
598 change in terms of group slope parameters were highly accurately re-
599 constructed over a wide range of non-Gaussian distributions. Therefore,

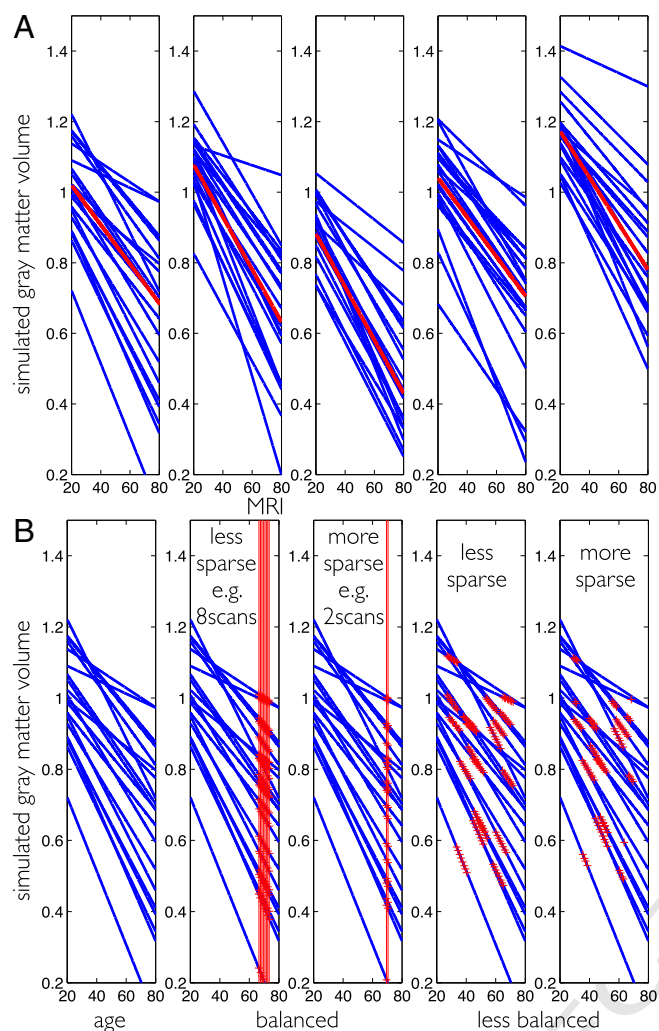


Fig. 2. Illustration of ground truth simulation for structural trajectories. (A) 5 random realizations of an ensemble of linear trajectories are plotted over the adult lifespan. Individual trajectories are shown in blue and the average trajectory is shown in red. (B) Illustration of simulated MRI acquisition. Ages of measurement t_{ij} are depicted by red crosses and red lines. Balanced designs (2 and 3 from left) vs. unbalanced (4 and 5 from left) and low (2nd from left) vs. high (3rd from left) sparsity of observations. Unbalanced sampling is illustrated using the age interval [20, 70] but see text for exact specification of the simulation.

the main model parameter seemed to be almost completely unbiased. Furthermore, our results show a slightly biased estimation of the hyperparameters under higher values of skewness and especially large values of kurtosis, i.e. peaked or super-Gaussian distributions. However, in our experience, strongly super-Gaussian data is rather unlikely in deformation based morphometric features, while more often slightly skewed data due to modulations from jacobian determinants is observed. Additionally, given the empirical results, the posterior uncertainty was stronger affected by the total variance differences of first and second level errors than by presence of significant higher central moments.

Finally, another possibility for evaluation and validation of our approach was used. We compared the linear Bayesian mixed-effects model to a simple summary statistic approach. The latter is generally valid if the design is balanced across subjects. That means that in this case the summary statistic approach should perform optimal, so we tested if our approach provides comparable results in this ideal scenario. As illustrated in Fig. 5, this idea was confirmed using a simulation framework with balanced and not age-balanced designs additionally varying the error variances. Our approach performed similar to summary

statistics for balanced designs over wide variety of first and second level error variances. We also observed that Bayesian mixed-effects models appeared more powerful than summary statistics when the latter is expected to be sub-optimal, i.e. in unbalanced designs. A similar result was obtained comparing balanced designs and varying timing of observations on the within-subject level (not shown).

Validation using real MRI data

Sample

In a second validation analysis, we provide a provisional assessment in terms of predictive validity by seeing if we could detect group differences (that we assume to be present). In this instance, we analyzed empirical data: The Bayesian mixed-effects models were applied and validated with a large longitudinal sample of healthy and pathological aging from the Alzheimer's Disease Neuroimaging Initiative (ADNI, <http://www.adni-info.org>)³ (see also Mueller et al., 2005).

We analyzed a subsample of the ADNI1 stage of the study, focusing on T1-weighted images acquired on 1.5 T scanners. After downloading and preprocessing 2397 scans of 474 participants, we excluded 39 subjects with 127 scans (due to substantial artifacts appearing in quality checks and errors during preprocessing). Apart from image sequence and preprocessing parameters (see also image preprocessing section), we did not apply any additional inclusion criteria.

The analyzed sample contained 2146 scans of 435 subjects, 181/254 female/male, ages 56.5–91.1, mean 76.4, std 6.7 years). The sample contains 10, 16, 31, 126, 113, 94, 43 and 2 subjects with ages 56–60, 60–65, 65–70, 70–75, 75–80, 80–85, 85–90 and 90–92 years respectively.

According to ADNI diagnostic criteria, the sample contained 688 scans of 140 healthy elderly subjects (further denoted as NO), 552 scans of 108 subjects with stable diagnosis of MCI during the whole ADNI study (denoted as sMCI), 530 scans of 92 subjects converting from original MCI diagnosis at baseline to AD during the ADNI study (pMCI), and 376 scans of 95 patients of patients diagnosed with AD.

The sample is less balanced with respect to age and the number of MRI acquisitions per subjects varies from 1 to 9 with 4.93 scans per subject on average. There were 34, 131, 122, 119 and 28 subjects having ≤ 3 , 4, 5, 6 and ≥ 7 scans respectively. Most MRI acquisitions were performed at baseline or 6, 12, 18, 24, 36, 48, and 60 months of the within subject study time. The sample maps within subject healthy and pathological aging from 17, 32, 126, 218, 40 and 2 elderly subjects over 0–1, 1–2, 2–3, 3–4, 4–5 and 5–6 years respectively. A more detailed description of the ADNI study design and sample selection procedures can be found at <http://adni.loni.usc.edu/data-samples/>.

³ Data used in the preparation of this article were obtained from the Alzheimer's Disease Neuroimaging Initiative (ADNI) database (adni.loni.usc.edu). The ADNI was launched in 2003 by the National Institute on Aging (NIA), the National Institute of Biomedical Imaging and Bioengineering (NIBIB), the Food and Drug Administration (FDA), private pharmaceutical companies and non-profit organizations, as a \$60 million, 5-year public-private partnership. The primary goal of ADNI has been to test whether serial magnetic resonance imaging (MRI), positron emission tomography (PET), other biological markers, and clinical and neuropsychological assessment can be combined to measure the progression of mild cognitive impairment (MCI) and early Alzheimer's disease (AD). Determination of sensitive and specific markers of very early AD progression is intended to aid researchers and clinicians to develop new treatments and monitor their effectiveness, as well as lessen the time and cost of clinical trials. The Principal Investigator of this initiative is Michael W. Weiner, MD, VA Medical Center and University of California – San Francisco. ADNI is the result of efforts of many co-investigators from a broad range of academic institutions and private corporations, and subjects have been recruited from over 50 sites across the U.S. and Canada. The initial goal of ADNI was to recruit 800 subjects but ADNI has been followed by ADNI-GO and ADNI-2. To date these three protocols have recruited over 1500 adults, ages 55 to 90, to participate in the research, consisting of cognitively normal older individuals, people with early or late MCI and people with early AD. The follow up duration of each group is specified in the protocols for ADNI-1, ADNI-2 and ADNI-GO. Subjects originally recruited for ADNI-1 and ADNI-GO had the option to be followed in ADNI-2. For up-to-date information, see <http://www.adni-info.org>.

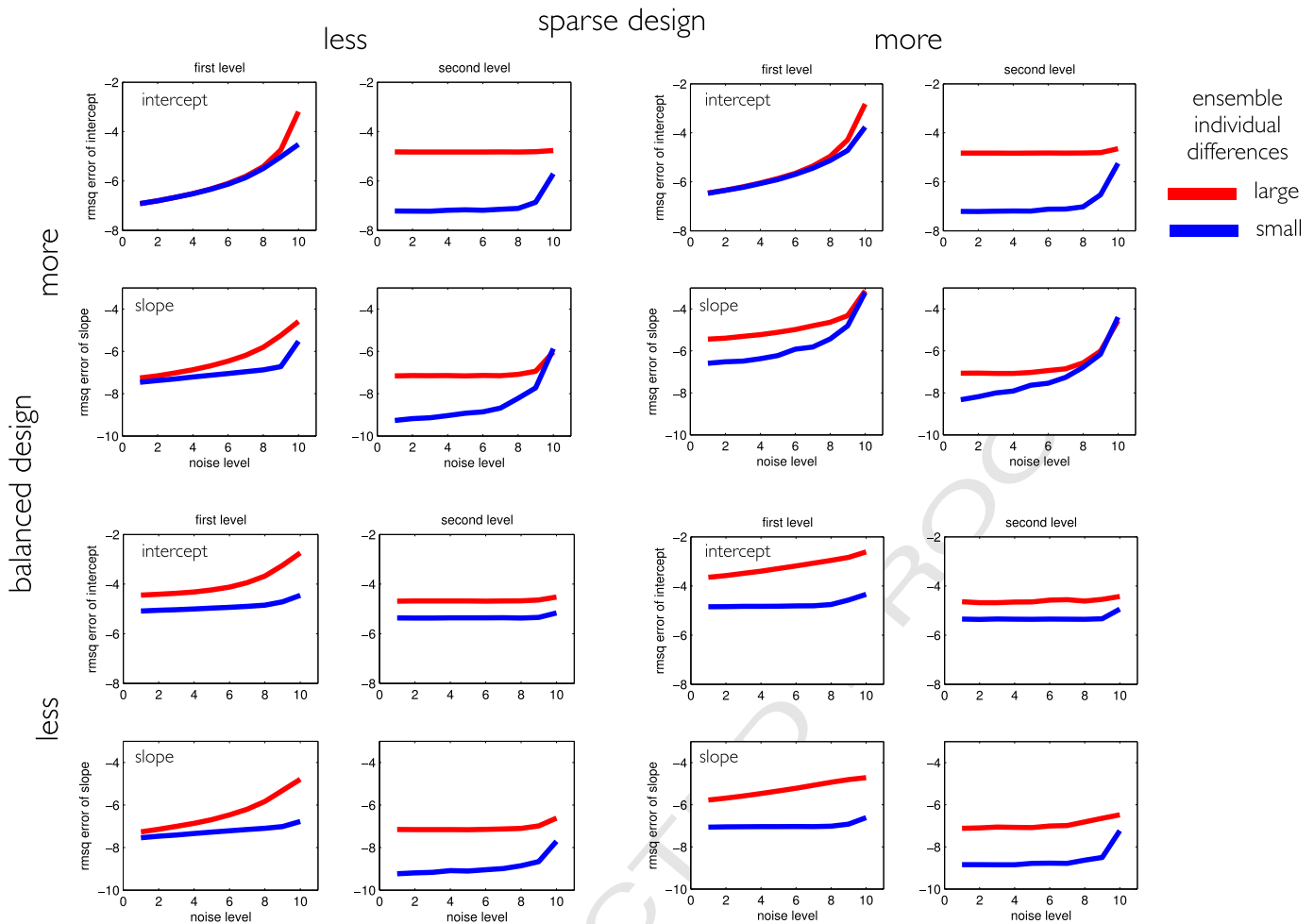


Fig. 3. Effects of design sparsity and having more or less balanced designs for first and second level model parameter estimation accuracy. All plots show log root mean squared errors (RMSQE) comparing ground truth vs. Bayesian model parameter estimates of intercept and slope for first (individual) and second (group) level. We manipulated the noise variance to follow $\sigma^2 = 0.01/(1 + 25 \times (p - 1)^2)$, with $p = 1, \dots, 10$ indicating the noise level. Red vs. blue lines indicate errors for large vs. small individual differences as a function of the first level noise parameter. Stronger noise mainly increases first level model errors. The log RMSQE is depicted for different designs with independent variation of loss of balance and sparsity. These results were obtained from averaging over 200 independent random realizations of the ensembles.

662 Symmetric diffeomorphic registration and image preprocessing

663 ADNI provides preprocessed T1-weighted images that have under-
 664 gone specific correction steps to reduce scanner induced biases. To re-
 665 duce these influences and minimize effects due to heterogeneity of
 666 protocols, all included images were chosen to match the MPRAGE
 667 with Gradwarp, B1 correction and N3 specification (see <http://adni.loni.usc.edu/methods/mri-analysis/mri-pre-processing/>). For further
 668 details about the applied ADNI MRI protocols please see <http://adni.loni.usc.edu/methods/documents/mri-protocols/>.

671 All further preprocessing steps were performed in SPM12b r6080
 672 (Wellcome Trust Centre for Neuroimaging, London, UK, <http://www.fil.ion.ucl.ac.uk/spm>). Because longitudinal MR-based morphometry is
 673 particularly prone to artifacts due to scanner inhomogeneities, registra-
 674 tion inconsistency, and subtle age-related deformations of the brains, it
 675 requires sophisticated preprocessing pipelines in order to detect the
 676 changes of interest and achieve unbiased results (Ashburner and
 677 Ridgway, 2013; Reuter and Fischl, 2011).

679 Thus, at first we applied the symmetric diffeomorphic registration
 680 for longitudinal MRI (Ashburner and Ridgway, 2013). In particular,
 681 this rests on an intra-subject modeling framework that combines non-
 682 linear diffeomorphic and rigid-body registration and further corrects
 683 for intensity inhomogeneity artifacts. The optimization is realized in a
 684 single generative model and is provides internally consistent estimates
 685 of within-subject brain deformations during the study period. The

686 registration model creates an average T1-image for each subject and
 687 the corresponding deformation fields for every individual scan.

688 Second, we applied SPM12b's unified segmentation to each subject's
 689 average T1-image, which assumes every voxel to be drawn from an un-
 690 known mixture of six distinct tissue classes: gray matter (GM), white
 691 matter (WM), and cerebrospinal fluid (CSF), bone, other tissue and air
 692 (see also Ashburner and Friston, 2005).

693 Third, all voxels within-subject average tissue maps were multiplied
 694 by the Jacobian determinants from the above longitudinal registration.
 695 Note, that this within-subject modulation is expected to encode all
 696 local individual volume changes during the study period.

697 Fourthly, nonlinear template generation and image registration was
 698 performed on the individual average GM and WM tissue maps using a
 699 geodesic shooting procedure (Ashburner and Friston, 2011). This de-
 700 fined the template space for all subsequent mixed-modeling steps.

701 Fifthly, the within-subject modulated (native space) segment im-
 702 ages were subsequently deformed to this study template space. Note
 703 that only within- but no between-subject modulation was applied. We
 704 further quality checked the ensuing images manually and using
 705 covariance-based inhomogeneity measures as implemented in the
 706 VBM8 toolbox for SPM.

707 Finally, images were smoothed using Gaussian kernels of 4 mm full
 708 width at half maximum. Subsequent modeling and analysis was per-
 709 formed for all tissue classes within corresponding binary masks. The

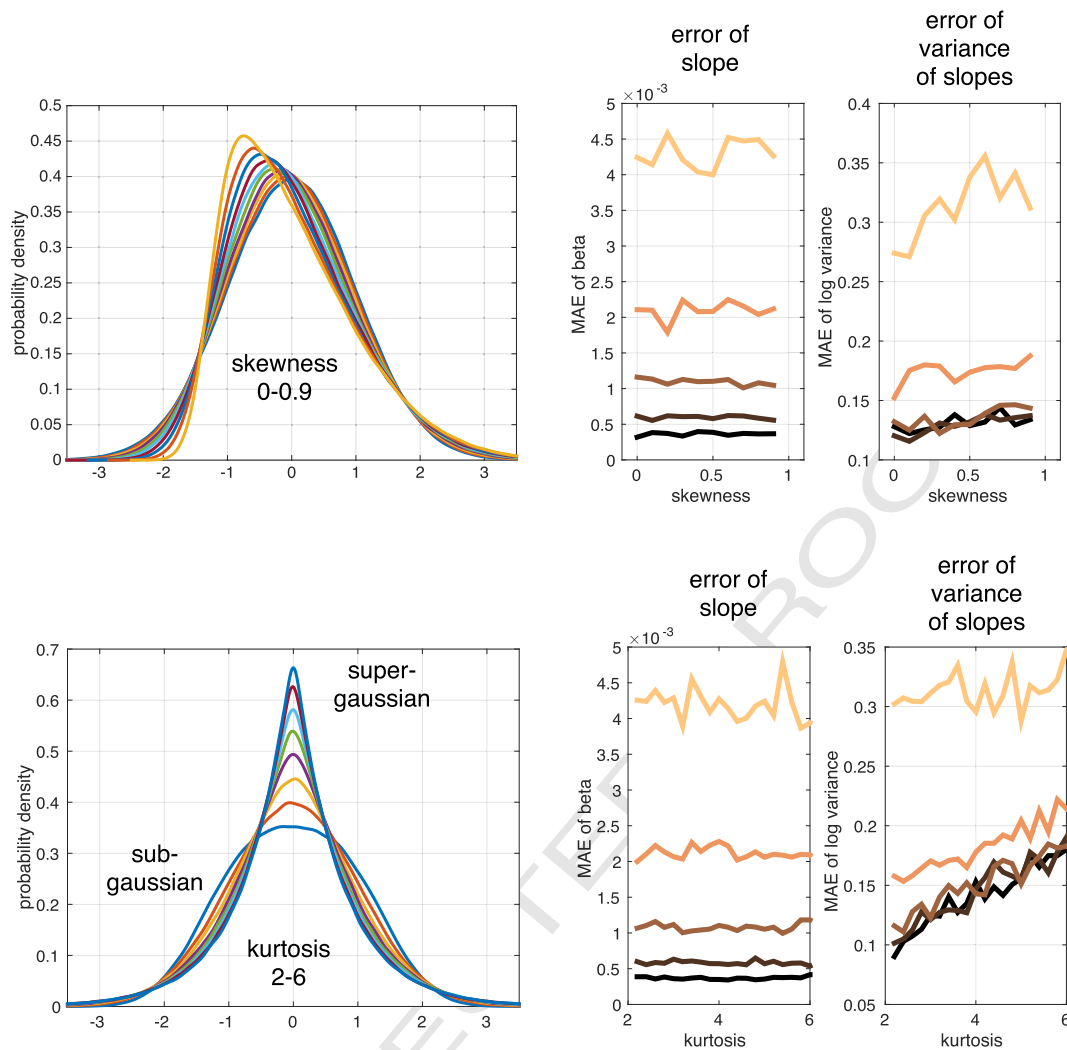


Fig. 4. Effects of non-gaussianity for second level slope parameter and hyperparameter estimation accuracy. Generalized normal distribution (type I and II) were used for generation of trajectory data with non-Gaussian first and second level errors. We simulated ensembles of 64 subjects with 5 annual scans per person. These were sampled under balanced/unbalanced designs and linear Bayesian mixed-effects model inversion was performed. Skewness (top row) and kurtosis (bottom row) were independently manipulated from mean and variance. Estimated slope parameter and hyperparameter were compared to ground truth values computing the mean absolute error (MAE) over 200 independent realizations. Brighter to darker shading of MAE in plots depicts increasing first level errors std of 0.01, 0.02, 0.04, 0.08, and 0.16 respectively.

710 masks were defined by a voxelwise sample mean of GM, WM and CSF
711 tissue maps exceeding an absolute threshold of 0.1, 0.4, and 0.2
712 respectively.

713 All mixed-effects modeling steps were performed on 1.5 mm resolu-
714 tion images of ADNI subsamples using the above steps. The resulting im-
715 ages are assumed to reflect age-related effects, as well as healthy and
716 pathological individual variability in terms of fine-grained maps of
717 local gray matter (GMV), white matter (WMV) and cerebrospinal fluid
718 volume (CSFV) content.

719 Computation time

720 Mass-univariate EM for Bayesian mixed-effects model inversion is
721 computationally expensive. Single voxel computation time was found
722 to depend on number of subjects, scans, groups, polynomial model de-
723 gree and number of covariates. Subgroup models using linear trajec-
724 tories ($N = 60$, $M = 300$, $G = 1$, $D = 1$, $R = 1$) took 4 h for local
725 estimation in whole brain gray matter regions (0.05 s per voxel) on a
726 desktop machine (6.5 CentOS Linux, Intel Xeon CPU, 3.20GHz, 12GB,
727 Matlab R2013b). Using large sample data like ADNI with many
728 hyperparameters, a single voxel inversion can take up to 30 s. However,
729 mass-univariate estimation lends itself nicely to parallel computation.

Using cluster computing facilities most model estimations were
730 achieved within 1–3 days. 731

732 Normal aging and comparison of clinical groups trajectories

733 First, we characterized trajectories in normal aging subjects. Fig. 6
734 shows PPMs of linear (i.e. slope) coefficients of the ensemble average
735 trajectory in our normal aging group. In particular the PPMs indicated
736 widespread decline of local volumes in GM and WM regions and sub-
737 stantial growth of CSF volume in the ventricles and sulcal regions.
738 Using this sensitive longitudinal design, almost all regions were found
739 to be affected by aging. Although the presented framework exploits lin-
740 ear mixed-effects models, one can explore nonlinear age-related effects
741 by inclusion of quadratic terms and model. Assuming a quadratic model
742 for every subject, we observe accelerated volume loss within many re-
743 gions from all lobes. Most prominent accelerations were found in tem-
744 poral GM and even more evident in the expansion of the lateral
745 ventricle.

746 To further validate our model, we next compared local structural tra-
747 jectories in clinical groups of the ADNI sample. Fig. 7 shows the PPMs of
748 slope comparisons of the sMCI, pMCI and AD groups against the slope in
749 the group of normal aging subjects (NO). The comparisons of clinical
750 and normal aging groups clearly indicate a region specific, tempo-

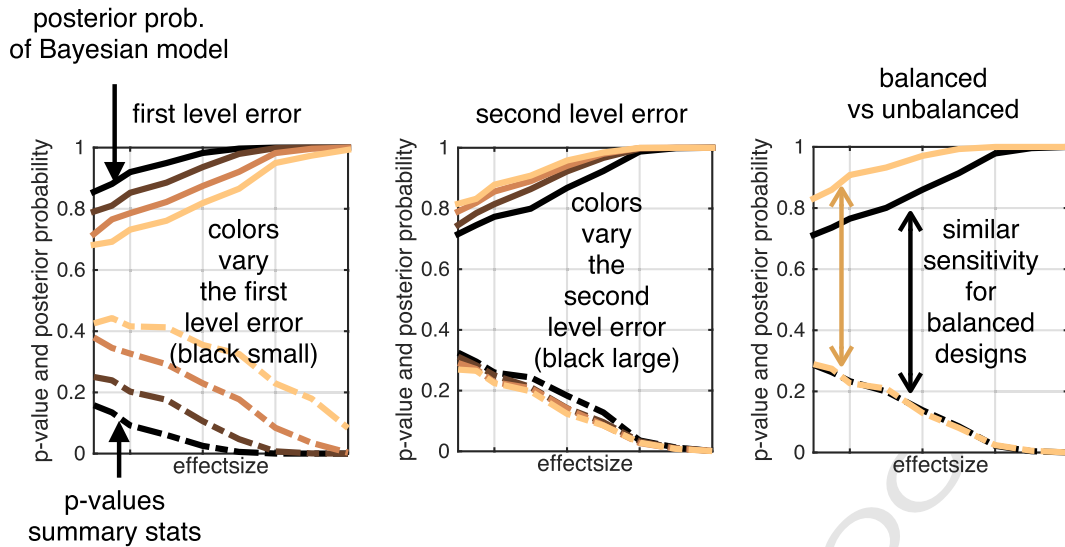


Fig. 5. Comparison of Bayesian mixed-effects model with summary statistics for detection of changes on the group level, i.e. finding a negative slope for different ground truth effect sizes. Posterior probabilities (upper part) and p-values from summary statistics (lower part) are shown under variations of first (left) and second (middle) level error variances and design types (right). Summary statistics here means using independent linear models for every subject and calculating p-values from a one-sample *t*-test of obtained slope parameters. Realizations of ensembles of 64 subjects with 5 annual scans per person. These were sampled under balanced/unbalanced designs and subsequently modeled. Balanced here means that every subject has the same average age at measurements while unbalanced means a uniform distribution of each subject's average age across the whole study interval [20, 80]. All probabilities are shown as a function of (from left to right increasing) ground truth effect size, i.e. increasing steepness of decline. Results are obtained from averaging across 200 realization of ensembles for each parameter configuration. Color shading indicates the manipulation of the variable of interest, i.e. error sizes (left and middle) and balanced design property (right). Here, p-values and posterior probabilities show similar dependence on effect sizes in balanced designs (see black curves right plot). Posterior probabilities show a gain of sensitivity when designs become unbalanced (see ochre curves right plot) while summary statistics perform similar for both designs. Probabilities in left and middle plot are average across multiple design types.

751 parietal pattern of increased rates of atrophy in GM and WM volumes.
 752 This pattern is complemented by an increased rate of ventricle expansion
 753 in the disease groups. Groups that develop a full AD pathology
 754 (pMCI and AD) also show more negative rates of atrophy in frontal,

occipital and cerebellar regions. Additionally to the more widespread
 755 spatial extent of the pathology in pMCI and AD compared to sMCI
 756 groups, the average rate of volume loss in terms of slope differences in-
 757 dicates a faster decline of regional temporo-parietal volume.
 758

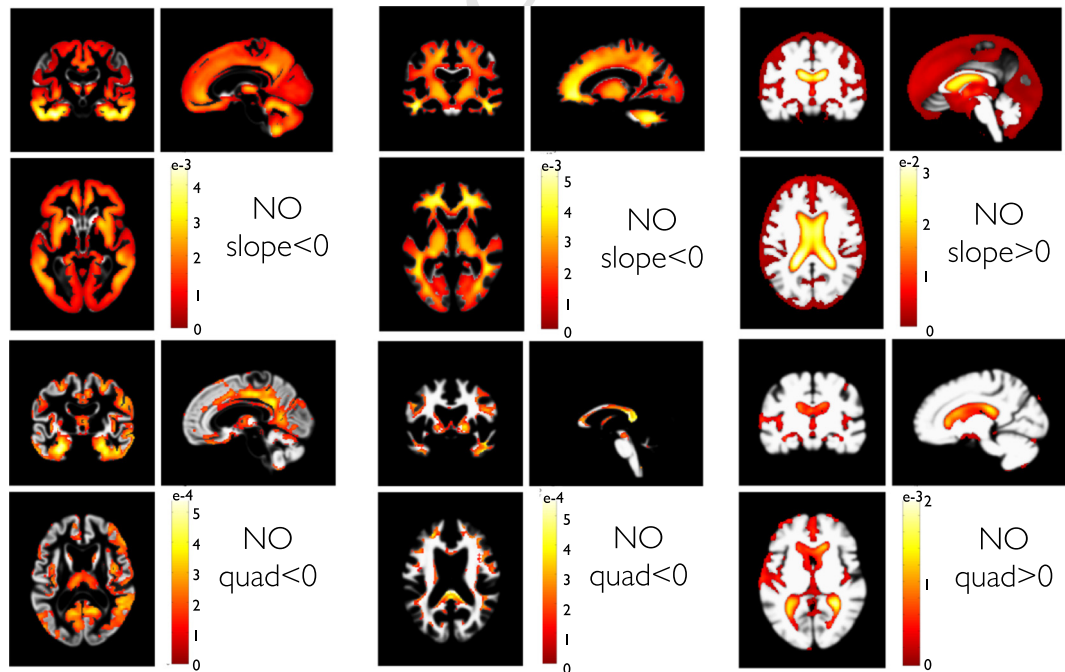


Fig. 6. Posterior probability maps of group trajectories in 140 normal aging subjects (denoted as NO). Posterior probability maps (PPMs) are shown for the slopes and quadratic components in a second order model with $D = 2$. The PPM enables regionally specific inferences about parameter contrasts $c^T\theta$ and are shown after thresholding: showing only voxels for which the posterior probability $p(c^T\theta > 0|y)$ exceeds the probability 0.95 (with contrast vector c defining the effect of interest). For this particular comparison, the contrasts c contained an entry of one (or minus one) for the corresponding linear (top row) and quadratic (bottom row) second level normal aging group parameters and zero elsewhere. That means slope (and quadratic) < 0 denotes tests for linear (quadratic) components being smaller than zero. Color bar scaling denotes parameter contrast values $c^T\theta$, i.e. the slope or quadratic coefficients. White or gray colored regions have posterior probabilities < 0.95 . The sign of the contrast is adapted to detect either decline in GM or growth in CSF volumes respectively. Columns depict PPMs of GM, WM and CSF tissue segments respectively.

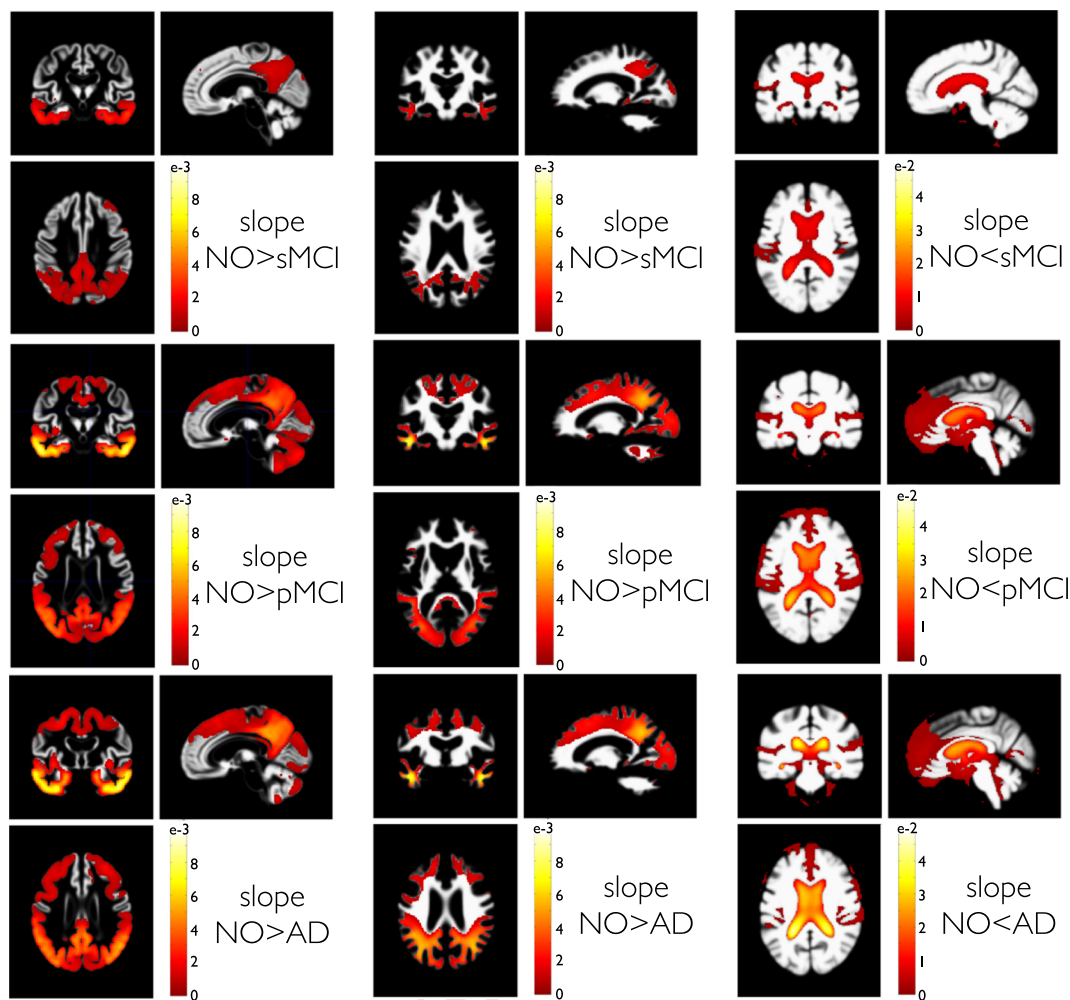


Fig. 7. PPMs of clinical group trajectories compared to normal aging. PPMs are shown for differences of trajectory slopes in groups of 108 sMCI (top row), 92 pMCI (middle row) and 95 AD (bottom row) subjects compared to slopes in the NO group with 140 subjects. As with directed comparisons using one-sided t-tests in GLM, here we only depict the contrast for steeper slopes in the clinical groups. This contrast addresses the hypothesis that AD and MCI pathology produces faster volume loss for GM and WM volumes and faster volume increase in CSF volumes compared to normal aging. Columns depict PPMs of GM, WM and CSF tissue maps respectively. Colors bars denote parameter contrast values $c^T\theta$, i.e. slope in NO minus slope in sMCI, pMCI and AD respectively. Because CSF shows growth, the sign of the contrast was reversed.

759 This conversion effect can be seen by evaluation of slope differences
 760 in pMCI and sMCI groups (Fig. 8). According to our sample, the conversion
 761 from MCI to AD at some point during the study also seems to be
 762 reflected in differential rates of local brain volume changes. Due to lim-
 763 itations of space, we restrict our presentation of comparisons to second
 764 level slope parameters. It is worth mentioning that the model supports

765 similar comparisons for the trajectory intercepts, which mainly reflect
 766 existing differences before the study, as opposed to ongoing changes
 767 of brain structure during the study. Three examples of individual struc-
 768 tural trajectories are shown in Fig. (9).

769 Examples of subject level and group level trajectories in NO, sMCI,
 770 and pMCI groups are displayed in Fig. 10. As expected for a hierarchical

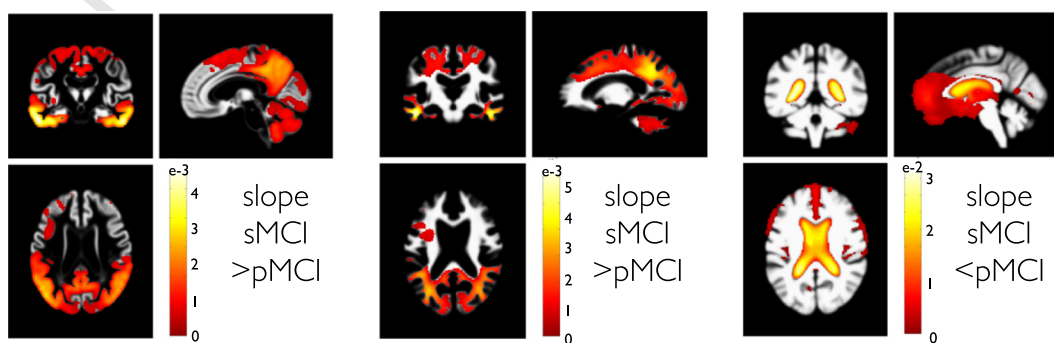


Fig. 8. PPMs of stable MCI compared to progressive MCI group trajectories. PPMs are shown for differences of trajectory slopes in a group of 108 sMCI compared to 92 pMCI subjects. Here, we focus on the contrast for steeper slopes in pMCI compared to sMCI. Columns depict PPMs of gray matter, white matter and CSF tissue maps respectively. Colors bars denote parameter contrast values $c^T\theta$, i.e. slope in sMCI minus slope in pMCI. Because CSF shows growth, the sign of the contrast was reversed.

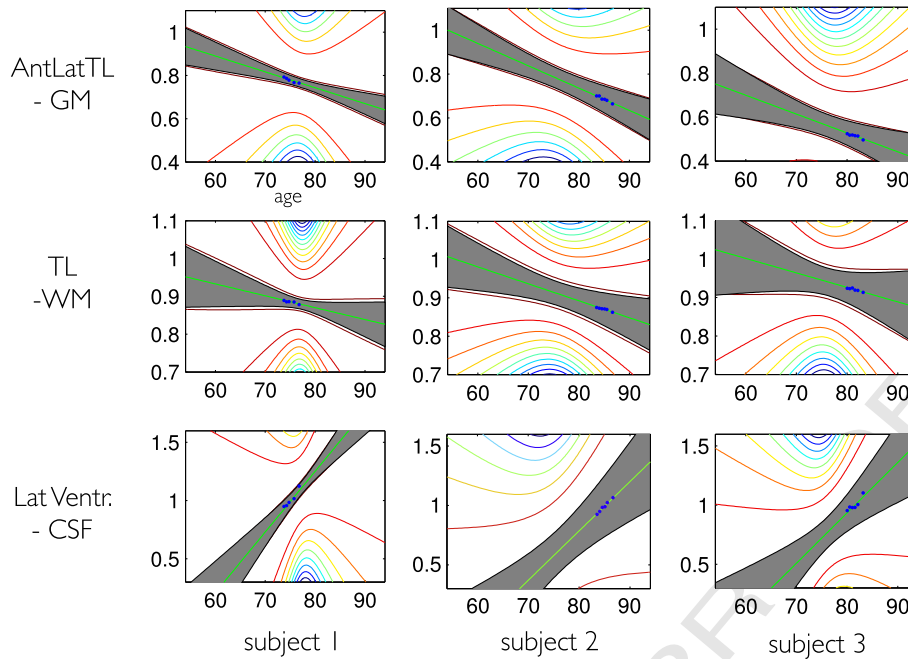


Fig. 9. Individual structural trajectories using a linear model. Three random subjects (1 NO, 1 sMCI, 1 pMCI) were chosen and we demonstrate local trajectories in three example voxels from the anterior lateral temporal lobe GM (upper row), temporal lobe WM (middle row), and lateral ventricle (bottom row). The observed data is shown in blue, the individual predicted trajectory $g(t, \theta^{(1)})$ is shown in green including the ± 2 standard deviation of its posterior uncertainty (gray area) and the contour plot of the uncertainty pdf outside the ± 2 std area. The uncertainty is mainly driven by the parametrization around the center of mass of age r_i in the whole group.

771 model, the posterior trajectory precision (or inverse variance) is found
 772 to be much smaller for the group level compared to the individual
 773 level. Ensemble trajectory estimates in groups are more precise and
 774 inference therefore more sensitive for detecting developmental
 775 differences.

Analysis of individual differences of trajectories

776

In contrast to typical cross-sectional MRI studies of brain develop- 777
 ment and aging, individual trajectory models, based on repeated mea- 778
 sures MRI, also afford analysis of within-subject change variability. A 779
 strength of our approach is that we can explore effects of risk or 780

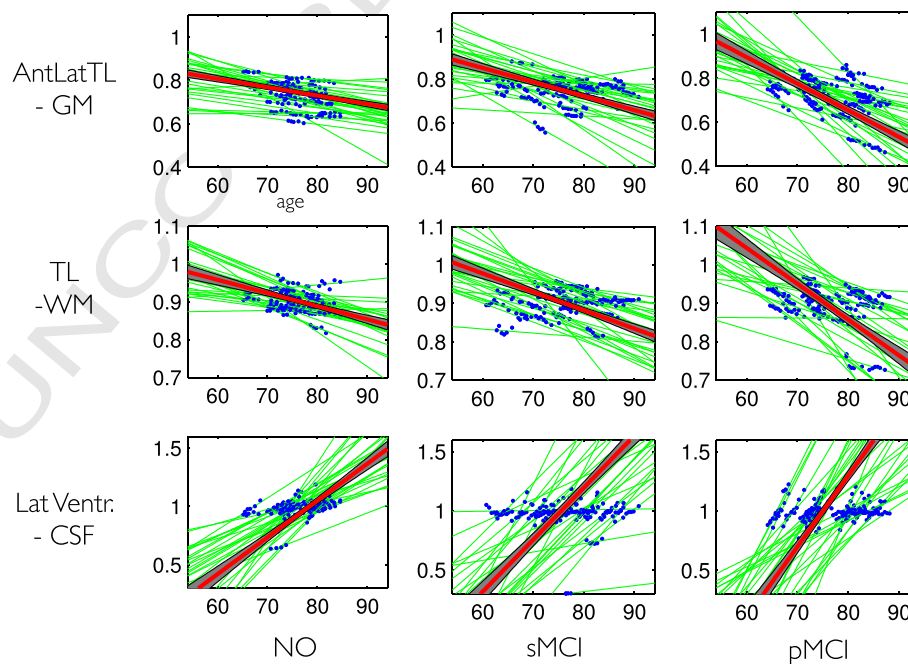


Fig. 10. Individual and group level structural trajectories using a linear model. Three single voxels (same as in 7) were chosen to demonstrate our local trajectory model: anterior lateral temporal lobe GM (upper row), temporal lobe WM (middle row), and lateral ventricle (bottom row). The observed data is shown in blue, the individual predicted trajectories $g(t, \theta^{(1)})$ are shown in green. The group average trajectories are shown in red attached with the ± 2 standard deviation of its posterior uncertainty (gray area). To improve visualization, only 30 individual trajectories (without uncertainty) are shown.

781 protective factors on ongoing structural decline. This could involve life-
782 style parameters, genetic profiles, cognitive test scores etc. or any stable
783 between-subject variable of interest.

784 To demonstrate the potential of this method, we focused on
785 explaining variability of local rates of atrophy based on the E4 allele of
786 the Apolipoprotein gene (further denoted as ApoE4), an established
787 risk factor for increased lifetime prevalence of AD. We define this
788 score as the number of ApoE4 allele of an individual, which can have either
789 zero, one or two copies. This risk score was entered as a predictor Z
790 (in Eq. (6)) for slope variability. Fig. 11 shows the PPMs for voxels showing
791 steeper decline of GMV (or growth of CSFV) with higher ApoE4 risk
792 in the group of NO and sMCI.

793 We observed localized effects indicating faster volume loss in anterior
794 or medial temporal lobe regions and lateral ventricle growth in normal
795 subjects with higher ApoE4 risk scores. More widespread effects were
796 found in temporo-parieto-frontal GM regions of stable MCI subjects. In
797 addition to the above between groups differences of change, these results
798 demonstrate the sensitivity of our method for analysis of additional
799 within-group heterogeneity of change.

800 Comparing models of different degrees

801 Here we demonstrate examples for evidence-based model compar-
802 ison within our generative trajectory modeling framework. There are
803 many questions in the context of longitudinal MRI studies that can be elegantly
804 framed in terms of model comparisons.

805 Firstly, one might aim at inference about different parametrizations,
806 particularly the choice of a certain polynomial model degree of random
807 and fixed effects of the trajectory models, i.e. the choice of $[D, D_f]$. This is
808 crucial in light of evidence for nonlinearities in brain maturation (Shaw
809 et al., 2008), accelerated gray matter loss in healthy aging (Fjell et al.,
810 2013) and other nonlinearities in clinical groups (Leung et al., 2013).

811 Secondly, one might also be interested in comparing generative
812 models using different sets of covariates, e.g. by including informative
813 predictors for individual differences of change. Fig. 12 gives an example
814 of log Bayes factors for linear and second order models obtained from
815 independent EM optimization for each model. Bayes factors in our normal
816 aging group clearly favor a linear random effects model over alterna-
817 tive models in most gray matter regions. Introducing age as a fixed
818 effect increased model evidence. Model evidence was further improved
819 by allowing for random slope variability in most gray matter regions, espe-
820 cially in medial temporal lobe regions. According to the same compar-
821 ison, individual differences among structural brain changes are
822 most pronounced in the lateral ventricle regions.

823 Interestingly, parts of the ventricles exhibited further increased
824 model evidence by additional inclusion of random quadratic growth ef-
825 fects. This was found to be emphasized for the lateral ventricle which in
826 parts borders on the hippocampus. We further evaluated models with
827 all combinations of fixed and random effects up to second order.

828 The overall winning model in most gray matter includes random ef-
829 fects for intercepts and slopes. Exceptions were found in right temporo-
830 parietal and postcentral gray matter regions, and in left inferior frontal
831 gyrus. Here and within parts of the lateral ventricle a quadratic random
832 effects model was more sufficiently for capturing individual differences
833 of change in normal aging.

834 Permutation testing for empirical false positive rate

835 Finally, to ensure our voxelwise estimation scheme does not pro-
836 duce spurious or misleading conclusions we repeated a similar analysis
837 under random permutations. We focussed on a subsample of 60 normal
838 subjects with 300 MRI scans. Similar effect maps as shown for the whole
839 group of normals were obtained. Then The data was randomly permuted
840 100 times and we reran the Bayesian model inversion outlined
841 above. Posterior probability maps were calculated exactly as outlined

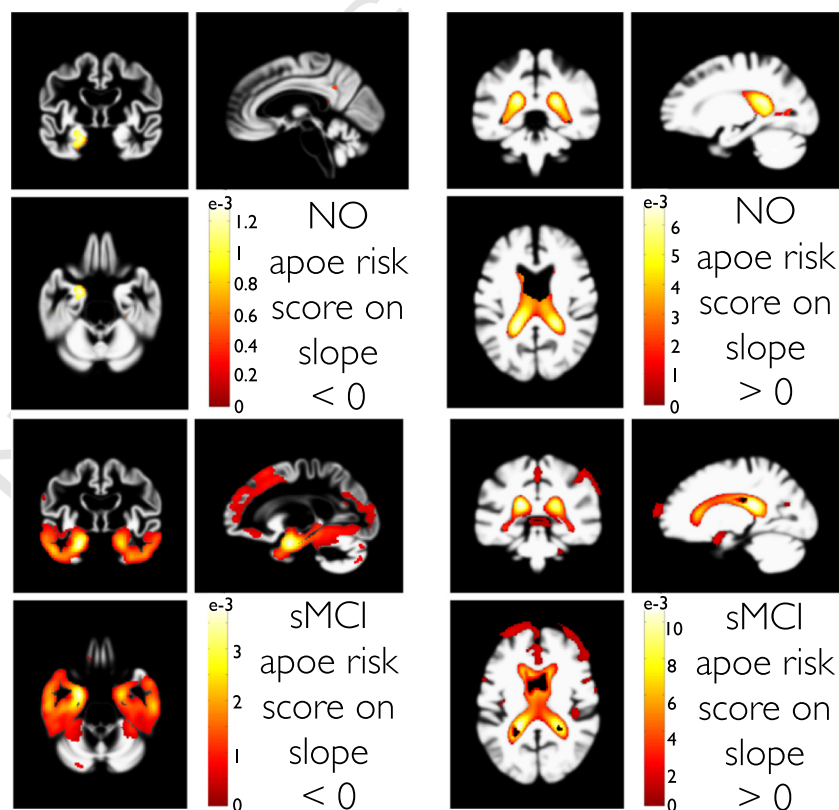


Fig. 11. Parametric analysis of trajectory slope variability using a ApoE4 risk score in NO (top row) and sMCI (bottom row) subjects. The applied ApoE4 risk score counts the number of ApoE4 allele, 0, 1, or 2 respectively. PPMs with contrasts for a steeper local GMV decline (left column) and CSFV growth (right column) with increased risk are shown. Colors bars denote parameter contrast values C_0 , with C containing a (minus) one for the ApoE4 regressor and zero elsewhere.

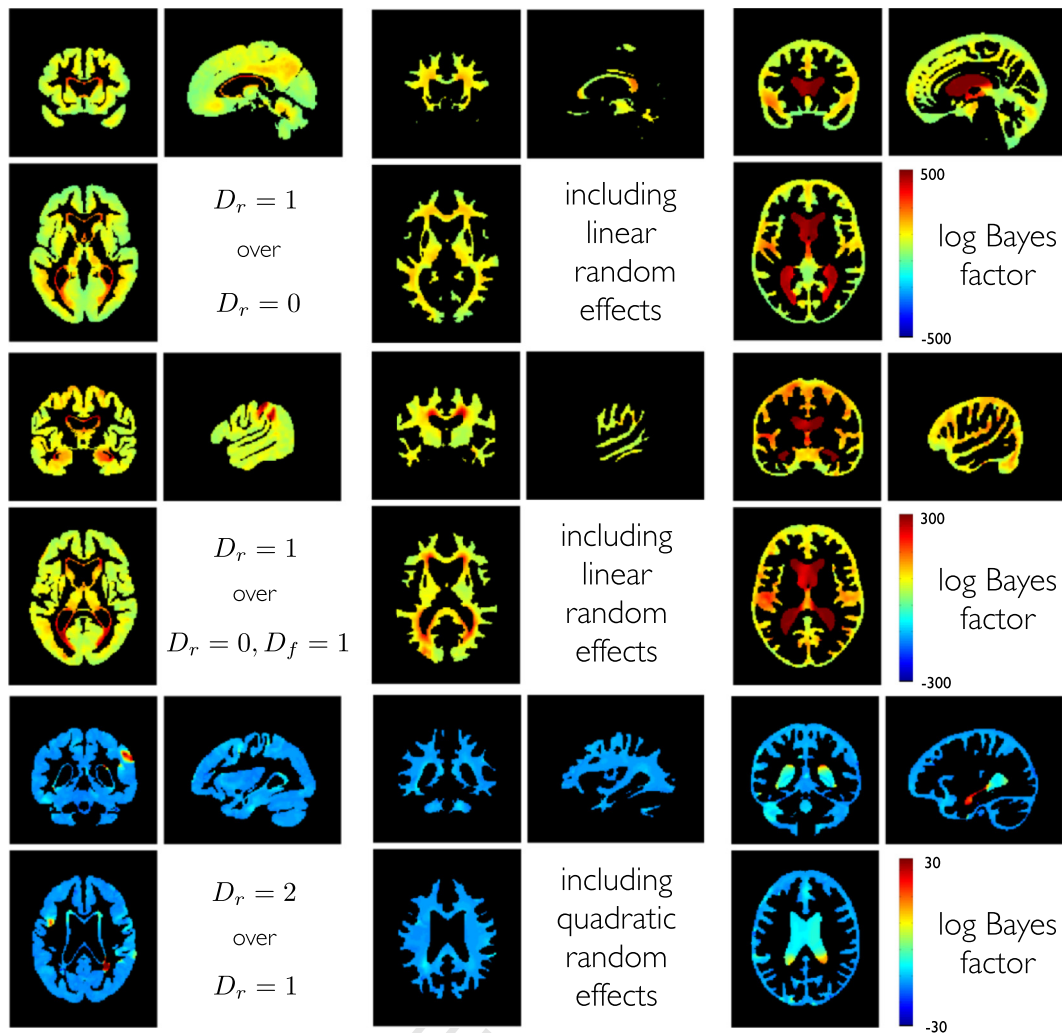


Fig. 12. Bayesian model comparison about polynomial degree within the normal aging group with $N = 140$. Top row shows log Bayes factors comparing a model with random intercepts and random slopes to a model with only random intercepts ($D_r = 1$ vs. $D_r = 0$). Middle row shows the comparison of a random intercept and random slope model to a random intercept model with fixed effects slope ($D_r = 1$ vs. $D_r = 0$, $D_f = 1$). Bottom row shows log Bayes factors comparing a full second order random effects model compared to a linear random effects model with random slopes and intercepts ($D_r = 2$ vs. $D_r = 1$). Columns show model comparisons separate for gray matter, white matter and CSF maps. Higher mixed-effect degrees were estimated but are not shown because of lower model evidence and limitations of space.

in the full ADNI model. We hoped to see that the number of voxels in the ensuing PPMs (thresholded at 95%) was 5% of the search volume or less. The mean false positive rate was found to be 2.85%. The distribution of % suprathreshold voxels over 100 presentations (with replacement) is shown in Fig. 13 (right). More generally, no indication for increased false positive rates was found for other probability thresholds as well (see Fig. 13 left).

Discussion

We have described, validated and applied a powerful framework for analysis of brain morphometry in longitudinal MRI data using Bayesian inference. The emphasis is on the analysis of individual differences of brain changes in one or more samples and subsequent inference about the contribution of subject specific covariates such as cognitive abilities, behavior, psychopathology, health, and lifestyle factors.

In particular, the approach exploits algorithms for within- (Ashburner and Ridgway, 2013) and between- (Ashburner and Friston, 2011) subject diffeomorphic registration in order to generate non-linearly registered tissue volume images of subjects and scans using Jacobian determinants of deformations. The resulting (modulated) tissue segment maps are subjected to mass-univariate generative mixed-effects modeling.

EM is used for Bayesian inversion of the generative model by estimating variance components and empirical Gaussian priors on individual differences of change. The model is hierarchical and provides estimates of local individual change trajectories over the whole study period, even for variable numbers of scans per subject or for less balanced designs.

Our approach is similar to recently proposed iterative schemes for surface-based cortical thickness analysis in longitudinal MRI data (Bernal-Rusiel et al., 2012, 2013) and fMRI group analysis (Chen et al., 2013). We also briefly compared our EM algorithm to the openly available mass-univariate mixed-effects algorithms from Freesurfer (<https://surfer.nmr.mgh.harvard.edu/fswiki/LinearMixedEffectsModels>) (Bernal-Rusiel et al., 2012) (not shown in results) using synthetic longitudinal data (from Validation using simulated structural trajectories section) with linear models and balanced data with Gaussian errors. We found convergence to the same group trajectory parameter estimates suggesting the validity of the applied iterative mixed-model schemes. However, a detailed evaluation of multiple approaches in multiple settings (a) including non-Gaussian error distributions (b) with both balanced and unbalanced designs (c) with linear and non-linear ground truth trajectories, is left for future work.

In contrast to the above methods, our model focuses on Bayesian inference on fixed- and random-effect parameters for individual and

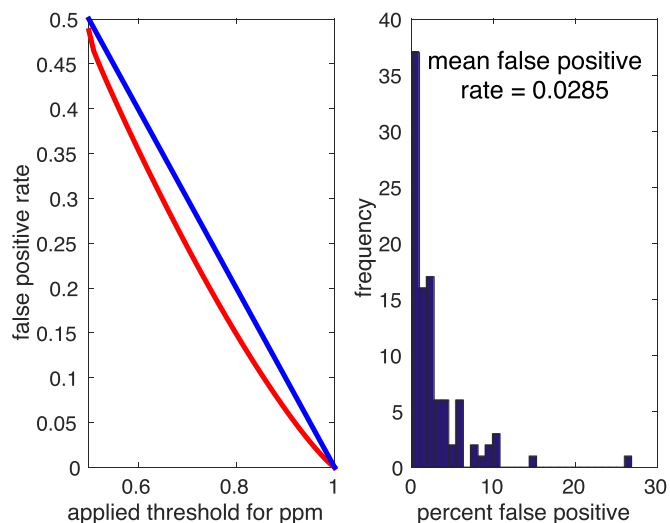


Fig. 13. Empirical false positive rate (red) obtained from permutation testing. We used 100 random permutations of a subset of 60 normal subjects with the original design and subsequently inverting the model including 300 000 gray matter voxels. Posterior probabilities were threshold using various thresholds (e.g. 0.95) and false positive rate was estimated as the number of above threshold voxels per volume averaged over the all permutations. The histogram of obtained false positive rate is shown right.

group trajectories, as well as Bayesian model selection. Our focus on Bayesian inference and random effects models overcomes some limitations of classical inference (for discussion see Friston et al., 2002a) and the proposed evidence based comparison of models allows one to navigate a rich model space.

Other Bayesian approaches for longitudinal MRI have been proposed with emphasis on either classification, evaluation of treatment effects, and dynamical networks (Elliott et al., 2010; Schmid et al., 2009; Chen et al., 2012). Our approach complements these methods by providing single subject trajectories and a model of their heterogeneity in aging samples. Notably, our iterative EM based random effects estimation also substantially differs from non-iterative marginal modeling using generalized estimation equations (for introduction see eg. Fitzmaurice et al., 2008) with recent application to longitudinal data using sandwich estimators (Guillaume et al., 2014) and adaptive multiscale methods (Skup et al., 2012).

We extensively validated our method using ground truth comparison with simulated longitudinal data. The model consistently reproduced veridical estimates across study designs with different characteristics. A design with fewer scans per subject was found to substantially reduce parameter accuracy, especially for the rates of change (or slopes). This result favors less sparse designs for efficient analysis of individual differences of change. Less balanced designs were also found to increase deviations from ground truth with some exceptions, especially for second level slope estimates and higher noise levels.

Notably, by construction, the design variability is part of the likelihood model and these effects are fully accounted for in the posterior parameter uncertainty (or credible intervals). Thus, using PPMs is expected to provide valid inference about individual, group and covariate parameters across a wide variety of study designs. Moreover, using non-Gaussian distributions, we have revealed some evidence for the robustness of the method under potential violations of the normality assumption. Mean parameter estimates were found to be unaffected from non-Gaussianity, hyperparameter were rather mildly affected by skewness and more biased by very large values of kurtosis. Comparison to valid summary statistics showed that posterior probabilities perform similarly in balanced designs and are likely to improve inference in typical unbalanced observational designs.

We further validated our approach using real MRI data from a large subsample of the available ADNI dataset. The spatio-temporal pattern of structural trajectories in subsamples for Normal Aging, stable MCI, progressive MCI and AD was found to be consistent with existing neuroimaging evidence (Driscoll et al., 2009; Misra et al., 2009; Anderson et al., 2012; Barnes et al., 2008; Vemuri et al., 2010b). Applying linear models of trajectories, PPMs of clinical groups indicated substantially increased rates of local brain atrophy and ventricle growth. The spatial pattern clearly emphasizes temporo-parietal regions in stable MCIs compared to normal aging, while higher rates of atrophy in pMCI and AD were also found in frontal gray matter regions. The sensitivity of this longitudinal mixed-modeling method was further demonstrated by observing differential rates of atrophy in progressive MCI compared to stable MCI. In line with recent evidence in healthy aging (Fjell et al., 2012), we also found additional accelerated decline (i.e. reverse U-shaped trajectories) of cortical and subcortical gray matter regions and accelerated growth (i.e. U-shaped trajectories) of lateral ventricle using quadratic models. As suggested by the study of (Holland et al., 2012), different patterns of change of rates of atrophy might apply to pathological compared to healthy aging groups. We will focus on the volume dynamics during disease progression in a separate paper.

Using ADNI data we also aimed to explore the strength of mixed-effects models to identify the effects of covariates of interest. For that particular purpose, we chose to analyze the effects of a genetic risk score based on the number of ApoE4 alleles, i.e. 0, 1, or 2, a well known and established risk factor for development of AD and corresponding signs of atrophy in MRI (Vemuri et al., 2010a; Risacher et al., 2010; Morgen et al., 2013; Taylor et al., 2014; Tosun et al., 2010; Moffat et al., 2000; Hostage et al., 2014). Although one could have alternatively used group comparisons based on number of ApoE4 alleles, we preferred to include this risk score as an example for an additional predictor of within group variability around the mean changes in normal aging and stable MCI groups.

The PPMs of ApoE4 risk's second level contrast indicated effects on variability of ventricle growth in normal aging and widespread effects on gray matter rate of atrophy in stable MCI. This emphasizes the risk score as an important contributing factor to local structural aging. Similarly, this technique could be used for parametric analysis of other risk scores or continuous behavioral variables thought to be involved in development and aging.

Candidate hypotheses about brain development and aging can be framed in terms of specific trajectory models. These hypotheses might involve (A) the inclusion of certain degrees of fixed or random effects of time, nonlinearities etc. and (B) explicitly modeling brain-behavior relationships by inclusion of behavioral covariates. Scientists can then use Bayesian inference to update their beliefs about the respective hypotheses, in light of new (neuroimaging) data.

Bayesian model selection has been introduced to identify the most likely of a set of hypotheses e.g. using log model evidence ratios or Bayes factors (Kass and Raftery, 1995). Evidence comparisons of nested models are analogous to the F-tests commonly used in Statistical Parametric Mapping (SPM) (Friston et al., 1995). However, a major advantage of applying Bayesian instead of frequentist inference to trajectory models is that evidence based comparison extends to non-nested models. This is useful because different combinations of random and fixed effects or covariates are not necessarily nested. For instance first order random effects models cannot be reduced to a zero order random effects model with first order fixed effects by setting some variables to zero.

Voxelwise model evidence maps were previously introduced for efficient group level inference in fMRI using random effects (Rosa et al., 2010). Our models extend this idea to mixed-effects models for longitudinal MRI. Using a normal aging sample, we here demonstrate that Bayesian model selection can be also used for particular choices of combinations of random and fixed effects in normal aging-related structural changes. We explored a model space with all combinations of fixed and

random effects up to order three. Pairwise comparisons of models were illustrated using Bayes factor maps.

The model with the most evidence was found to vary over regions and tissue classes. For most gray matter regions a random intercept and slope model was found to be most likely, with exceptions of a left prefrontal and a postcentral region, and regions adjacent to the ventricles. These were found to show second order random effects with individual differences of accelerations.

The second order random effects model was also more likely for the lateral ventricle adjacent to the hippocampus and its posterior parts. Although we only found accelerated lateral ventricle volume increases, this is in line with recent observations of late accelerated aging in hippocampal gray matter in normal aging (Ziegler et al., 2012b; Fjell et al., 2012). Disregarding potential segmentation difficulties of hippocampal gray matter, one also might expect that the spatial regularization of the within-subject deformations is slightly biased towards the adjacent ventricle growth. This might have reduced the sensitivity for detection of second order individual decline differences in hippocampal regions.

At the same time, our results extend existing fixed effects findings. Similar to a recent study using ROIs from manual volumetry (Raz et al., 2010), mixed-effects models go beyond testing for (nonlinear) fixed effects of aging because they explicitly model heterogeneity of structural changes.

In contrast to findings of Raz et al. (2010), where some regions did exhibit age-related change, but without any sign of individual differences, here Bayesian model selection showed the highest model evidence for linear or even quadratic random effects. In fact, in our voxelwise whole brain search we did not observe any brain region in all three analyzed tissue classes that exhibited most evidence for a model with random intercepts and linear fixed effects, i.e. showing uniform aging across subjects. These deviations of semi-automated and manual longitudinal volumetry might be further addressed.

Our ADNI sample findings suggest substantial heterogeneity among local structural brain changes in normal aging subjects without (or prior to) signs of dementia. Similar questions might be addressed about the heterogeneity of trajectories in disease states and during treatment processes.

It is also worth mentioning that the optimal degree of random effects (from evidence based comparison) specifies the dimensionality of individual differences in aging brain structure. This degree determines the complexity of a sufficient individual model of change rather than only quantifying the smoothness of the temporal dynamic on the group level. This idea nicely connects to the multivariate perspective on cognitive ability differences (see e.g. Ziegler et al., 2013).

Future studies might focus on Bayesian model selection in larger random effects model spaces using additional sets of genetic, physiological, and behavioral predictors. After sufficiently capturing the complexity of individual differences of aging-related brain changes as random effects (or hidden variables), one might aim to explain latent variables based on other observations, such as behavior, genes, and other MRI modalities.

Here we applied uninformative priors in the presented results. However, the proposed framework enables flexible specification of prior structures at the top-level of parameters, which can be used to implement prior knowledge about the process of interest, e.g. in terms of expected growth or decline rates in development or aging. The framework (and the corresponding implementation in SPM) will provide the choice of top-level priors being either uninformative (i.e. flat) or informative. Uninformative priors can be used for exploratory research similar to other standard mixed-effects models, while otherwise, informative priors can be chosen to be either fixed (for fully Bayesian inference) or estimated from the data using empirical Bayes. In particular, further extensions aim to include examples of empirical priors, e.g. global shrinkage or atlas-based regional shrinkage priors which regularize all voxelwise trajectory estimates after estimating a top level prior on the whole brain or regional ROI level respectively. The use of empirical

priors in context of neuroimaging data was recently motivated by machine learning applications showing the potential for probabilistic single case inference given the 'prior-knowledge' of a large MRI database (Ziegler et al., 2014). Although we did not observe any evidence for increased rates of false positives during permutation testing, it is worth mentioning that empirical priors have also been discussed in the context of control of false discovery rate (FDR) (Schwartzman et al., 2009).

We finally like to mention some limitations and possible extensions of this work. Firstly, Bayesian model reduction has been recently proposed for efficient inference on general linear models and dynamical systems models of neuroimaging data (Friston and Penny, 2011; Penny and Ridgway, 2013). Using model reduction, posterior estimates and model evidences might be accurately approximated for large model spaces using only the optimized full model (instead of inverting every reduced model). Future studies might therefore work on efficient approximation techniques to improve the efficiency of Bayesian model comparison across wider spaces of mixed-effects models.

Secondly, our presented model applied group specific priors with independent estimation of multiple ensembles of trajectories. However, the hierarchical modeling framework naturally extends to higher levels. These could be extended to model individual differences of changes in multiple clinical groups of a joint population, the inclusion of multi-center scanner levels, and the variance across birth cohorts.

Thirdly, the mass-univariate Bayesian model inversion is computationally very expensive and does not account for spatial correlations among the voxels. As in recent work, the model might be extended to combine priors on heterogeneity and image space using full spatio-temporal-models or adaptive smoothing techniques (see e.g. Bernal-Rusiel et al., 2013; Skup et al., 2012).

Finally, recently developed techniques in quantitative imaging provide biologically relevant properties, e.g. about brain myelination and iron levels (Draganski et al., 2011; Callaghan et al., 2014; Lambert et al., 2013). Following quantitative biomarkers in healthy and pathological development might be expected to provide biologically meaningful models of developmental heterogeneity while reducing the potential influence of anatomical shape variability.

Acknowledgments

We are grateful to John Ashburner for discussions, support, comments and corrections to the manuscript. This work was supported in part by the German Academic Exchange Service (DAAD). Data collection and sharing for this project was funded by the Alzheimer's Disease Neuroimaging Initiative (ADNI) (National Institutes of Health Grant U01 AG024904) and DOD ADNI (Department of Defense award number W81XWH-12-2-0012). ADNI is funded by the National Institute on Aging, the National Institute of Biomedical Imaging and Bioengineering, and through generous contributions from the following: Alzheimer's Association; Alzheimer's Drug Discovery Foundation; Araclon Biotech; BioClinica, Inc.; Biogen Idec Inc.; Bristol-Myers Squibb Company; Eisai Inc.; Elan Pharmaceuticals Inc.; Eli Lilly and Company; EuroImmun; F. Hoffmann-La Roche Ltd and its affiliated company Genentech, Inc.; Fujirebio; GE Healthcare; IXICO Ltd.; Janssen Alzheimer Immunotherapy Research & Development, LLC.; Johnson & Johnson Pharmaceutical Research & Development LLC.; Medpace, Inc.; Merck & Co., Inc.; Meso Scale Diagnostics, LLC.; NeuroRx Research; Neurotrack Technologies; Novartis Pharmaceuticals Corporation; Pfizer Inc.; Piramal Imaging; Servier; Synarc Inc.; and Takeda Pharmaceutical Company. The Canadian Institutes of Health Research is providing funds to support ADNI clinical sites in Canada. Private sector contributions are facilitated by the Foundation for the National Institutes of Health (<http://www.fnih.org>). The grantee organization is the Northern California Institute for Research and Education, and the study is coordinated by the Alzheimer's Disease Cooperative Study at the University of California, San Diego. ADNI data are disseminated by the Laboratory for Neuro Imaging at the University of Southern California. Dr Ridgway is supported

1120 by the Medical Research Council [grant number MR/J014257/1]. The
1121 Wellcome Trust Centre for Neuroimaging is supported by core funding
1122 from the Wellcome Trust [grant number 091593/Z/10/Z].

1123

1124 **Conflict of interest statement**

1125

1126 **Q4:** The authors declare that there are neither actual nor potential con-
1127 flicts of interest.

1128 **References**

1129 Anderson, V.M., Schott, J.M., Bartlett, J.W., Leung, K.K., Miller, D.H., Fox, N.C., 2012. Gray
1130 matter atrophy rate as a marker of disease progression in AD. *Neurobiol. Aging* 33
1131 (7), 1194–1202.

1132 Ashburner, J., Friston, K.J., 2005. Unified segmentation. *NeuroImage* 26 (3), 839–851.

1133 Ashburner, J., Friston, K.J., 2011. Diffeomorphic registration using geodesic shooting and
1134 Gauss–Newton optimisation. *NeuroImage* 55 (3), 954–967.

1135 Ashburner, J., Ridgway, G.R., 2013. Symmetric diffeomorphic modeling of longitudinal
1136 structural MRI. *Front. Neurosci.* 6.

1137 Barnes, J., Schill, R.L., Frost, C., Schott, J.M., Rossor, M.N., Fox, N.C., 2008. Increased hippo-
1138 campal atrophy rates in AD over 6 months using serial MR imaging. *Neurobiol. Aging*
1139 29 (8), 1199–1203.

1140 Barnes, J., Ridgway, G.R., Bartlett, J., Henley, S.M.D., Lehmann, M., Hobbs, N., Clarkson, M.J.,
1141 MacManus, D.G., Ourselin, S., Fox, N.C., 2010. Head size, age and gender adjustment in
1142 MRI studies: a necessary nuisance? *NeuroImage* 53 (4), 1244–1255.

1143 Bernal-Rusiel, J.L., Greve, D.N., Reuter, M., Fischl, B., Sabuncu, M.R., for the Alzheimer's
1144 Disease Neuroimaging Initiative, 2012. Statistical analysis of longitudinal neuroimaging
1145 data with Linear Mixed Effects models. *NeuroImage* 66C, 249–260.

1146 Bernal-Rusiel, J.L., Reuter, M., Greve, D.N., Fischl, B., Sabuncu, M.R., Initiative, A.D.N., 2013.
1147 Spatiotemporal linear mixed effects modeling for the mass-univariate analysis of lon-
1148 gitudinal neuroimaging data. *NeuroImage* 81, 358–370.

1149 Bishop, C.M., 2006. *Pattern Recognition and Machine Learning*. Springer.

1150 Callaghan, M.F., Freund, P., Draganski, B., Anderson, E., Cappelletti, M., Chowdhury, R.,
1151 Diedrichsen, J., Fitzgerald, T.H.B., Smittenaar, P., Helms, G., Lutti, A., Weiskopf, N.,
1152 2014. Widespread age-related differences in the human brain microstructure
1153 revealed by quantitative magnetic resonance imaging. *Neurobiol. Aging* 35 (8),
1154 1862–1872.

1155 Carmichael, O., Schwarz, C., Drucker, D., Fletcher, E., Harvey, D., Beckett, L., Jack, C.R.,
1156 Weiner, M., DeCarli, C., the Alzheimer Disease Neuroimaging Initiative, 2010. Longitudi-
1157 nal changes in white matter disease and cognition in the first year of the Alzheimer
1158 disease neuroimaging initiative. *Arch. Neurol.* 67 (11), 1370–1378.

1159 Chan, D., Janssen, J.C., Whitwell, J.L., Watt, H.C., Jenkins, R., Frost, C., Rossor, M.N., Fox, N.C.,
1160 2003. Change in rates of cerebral atrophy over time in early-onset Alzheimer's dis-
1161 ease: longitudinal MRI study. *Lancet* 362 (9390), 1121–1122.

1162 Chen, R., Resnick, S.M., Davatzikos, C., Herskovits, E.H., 2012. Dynamic Bayesian network
1163 modeling for longitudinal brain morphometry. *NeuroImage* 59 (3), 2330–2338.

1164 Chen, G., Saad, Z.S., Britton, J.C., Pine, D.S., Cox, R.W., 2013. Linear mixed-effects modeling
1165 approach to fMRI group analysis. *NeuroImage* 73, 176–190.

1166 Chetelat, G. a, Baron, J.-C., 2003. Early diagnosis of Alzheimer's disease: contribution of
1167 structural neuroimaging. *NeuroImage* 18 (2), 525–541.

1168 Debette, S., Seshadri, S., Beiser, A., Au, R., Himali, J.J., Palumbo, C., Wolf, P.A., DeCarli, C.,
1169 2011. Midlife vascular risk factor exposure accelerates structural brain aging and
1170 cognitive decline. *Neurology* 77 (5), 461–468.

1171 Dempster, A.P., Laird, N.M., Rubin, D.B., 1977. Maximum likelihood from incomplete data
1172 via the EM algorithm. *J. R. Stat. Soc. Ser. B (Stat Methodol.)* 39 (1), 1–38.

1173 den Heijer, T., van der Lijn, F., Ikram, A., Koudstaal, P.J., van der Lugt, A., Krestin, G.P.,
1174 Vrooman, H.A., Hofman, A., Niessen, W.J., Breteler, M.M.B., 2012. Vascular risk factors,
1175 apolipoprotein E, and hippocampal decline on magnetic resonance imaging over a
1176 10-year follow-up. *Alzheimers Dement.* 8 (5), 417–425.

1177 Donohue, M.C., Jacqmin-Gadda, H., Le Goff, M., Thomas, R.G., Raman, R., Gamst, A.C.,
1178 Beckett, L.A., Jack, C.R., Weiner, M.W., Dartigues, J.-F., Aisen, P.S., Initiative, A.D.N.,
1179 2014. Estimating long-term multivariate progression from short-term data.
1180 *Alzheimers Dement.* <http://dx.doi.org/10.1016/j.jalz.2013.10.003>.

1181 Douaud, G., Refsum, H., de Jager, C.A., Jacoby, R., Nichols, T.E., Smith, S.M., 2013. Preventing Alzheimer's disease-related gray matter atrophy by B-vitamin treat-
1182 ment. *Proc. Natl. Acad. Sci. U. S. A.* 110 (23), 9523–9528.

1183 Draganski, B., Ashburner, J., Hutton, C., Kherif, F., Frackowiak, R.S.J., Helms, G., Weiskopf, N., 2011. Regional specificity of MRI contrast parameter changes in normal ageing
1184 revealed by voxel-based quantification (VBQ). *NeuroImage* 55 (4), 1423–1434.

1185 Driscoll, I., Davatzikos, C., An, Y., Wu, X., Shen, D., Kraut, M., Resnick, S.M., 2009. Longitudi-
1186 nal pattern of regional brain volume change differentiates normal aging from MCI.
1187 *Neurology* 72 (22), 1906–1913.

1188 Elliott, C., Francis, S.J., Arnold, D.L., Collins, D.L., Arbel, T., 2010. Bayesian classification of
1189 multiple sclerosis lesions in longitudinal MRI using subtraction images. *Med. Image*
1190 *Comput. Comput. Assist. Interv.* 13 (Pt 2), 290–297.

1191 Fitzmaurice, G., Davidian, M., Verbeke, G., Molenberghs, G., 2008. *Longitudinal Data*
1192 *Analysis*. CRC Press.

1193 Fjell, A.M., Walhovd, K.B., 2010. Structural brain changes in aging: courses, causes and
1194 cognitive consequences. *Rev. Neurosci.* 21 (3), 187–221.

1195 Fjell, A.M., Westlye, L.T., Grydeland, H., Amlien, I., Espeseth, T., Reinvang, I., Raz, N., Dale,
1196 A.M., Walhovd, K.B., the Alzheimer Disease Neuroimaging Initiative, 2012.
1197 Accelerating cortical thinning: unique to dementia or universal in aging? *Cereb.*
1198 *Cortex* <http://dx.doi.org/10.1093/cercor/bhs379>.

1201 Fjell, A.M., Westlye, L.T., Grydeland, H., Amlien, I., Espeseth, T., Reinvang, I., Raz, N.,
1202 Holland, D., Dale, A.M., Walhovd, K.B., Alzheimer Disease Neuroimaging Initiative,
1203 2013. Critical ages in the life course of the adult brain: nonlinear subcortical aging.
1204 *Neurobiol. Aging* 34 (10), 2239–2247.

1205 Fonteijn, H.M., Modat, M., Clarkson, M.J., Barnes, J., Lehmann, M., Hobbs, N.Z., Schill, R.L.,
1206 Tabrizi, S.J., Ourselin, S., Fox, N.C., Alexander, D.C., 2012. An event-based model for
1207 disease progression and its application in familial Alzheimer's disease and
1208 Huntington's disease. *NeuroImage* 60 (3), 1880–1889.

1209 Frisoni, G.B., Fox, N.C., Jack, C.R., Scheltens, P., Thompson, P.M., 2010. The clinical use of
1210 structural MRI in Alzheimer disease. *Nature reviews. Neurology* 6 (2), 67–77.

1211 Friston, K.J., Penny, W., 2003. Posterior probability maps and SPMs. *NeuroImage* 19 (3),
1212 1240–1249.

1213 Friston, K.J., Penny, W.D., 2011. Post hoc Bayesian model selection. *NeuroImage* 56 (4),
1214 2089–2099.

1215 Friston, K.J., Holmes, A., Worsley, K.J., 1995. Statistical parametric maps in functional im-
1216 aging: a general linear approach. *Hum. Brain Mapp.* 2, 189–210.

1217 Friston, K.J., Penny, W., Phillips, C., Kiebel, S., Hinton, G., Ashburner, J., 2002a. Classical and
1218 Bayesian inference in neuroimaging: theory. *NeuroImage* 16 (2), 465–483.

1219 Friston, K.J.K., Glaser, D.E.D., Henson, R.N.A.R., Kiebel, S.S., Phillips, C.C., Ashburner, J.J.,
1220 2002b. Classical and Bayesian inference in neuroimaging: applications. *NeuroImage*
1221 16 (2), 29–29.

1222 Friston, K., Mattout, J., Trujillo-Barreto, N., Ashburner, J., Penny, W., 2007. Variational free
1223 energy and the Laplace approximation. *NeuroImage* 34 (1), 220–234.

1224 Frost, C., Kenward, M.G., Fox, N.C., 2004. The analysis of repeated 'direct' measures of
1225 change illustrated with an application in longitudinal imaging. *Stat. Med.* 23 (21),
1226 3275–3286.

1227 Grady, C., 2012. The cognitive neuroscience of ageing. *Nat. Rev. Neurosci.* 13 (7), 491–505.

1228 Guillaume, B., Hua, X., Thompson, P.M., Waldorp, L., Nichols, T.E., Initiative, A.D.N., 2014.
1229 Fast and accurate modelling of longitudinal and repeated measures neuroimaging
1230 data. *NeuroImage* 94, 287–302.

1231 Harville, D.A., 1977. Maximum likelihood approaches to variance component estimation
1232 and to related problems. *J. Am. Stat. Assoc.* 72 (358), 320–338.

1233 Holland, D., Dale, A.M., Initiative, A.D.N., 2011. Nonlinear registration of longitudinal
1234 images and measurement of change in regions of interest. *Med. Image Anal.* 15 (4),
1235 489–497.

1236 Holland, D., Desikan, R.S., Dale, A.M., McEvoy, L.K., Initiative, A.D.N., 2012. Rates of decline
1237 in Alzheimer disease decrease with age. *PLoS One* 7 (8), e42325.

1238 Hostage, C.A., Choudhury, K.R., Murali Doraiswamy, P., Petrella, J.R., Initiative, A.D.N.,
1239 2014. Mapping the effect of the apolipoprotein E genotype on 4-year atrophy rates
1240 in an Alzheimer disease-related brain network. *Radiology* 271 (1), 211–219.

1241 Jedynak, B.M., Lang, A., Liu, B., Katz, E., Zhang, Y., Wyman, B.T., Raunig, D., Jedynak, C.P.,
1242 Caffo, B., Prince, J.L., Initiative, A.D.N., 2012. A computational neurodegenerative
1243 disease progression score: method and results with the Alzheimer's disease Neuro-
1244 imaging Initiative cohort. *NeuroImage* 63 (3), 1478–1486.

1245 Kass, R.E., Raftery, A.E., 1995. Bayes factors. *J. Am. Stat. Assoc.* 90 (430), 773–795.

1246 Kempton, M.J., Ettinger, U., Schmechtig, A., Winter, E.M., Smith, L., McMorris, T.,
1247 Wilkinson, I.D., Williams, S.C.R., Smith, M.S., 2009. Effects of acute dehydration on
1248 brain morphology in healthy humans. *Hum. Brain Mapp.* 30 (1), 291–298.

1249 Lambert, C., Chowdhury, R., Fitzgerald, T., Fleming, S.M., Lutti, A., Draganski, B.,
1250 Frackowiak, R., Ashburner, J., 2013. Characterizing aging in the human brainstem
1251 using quantitative multimodal MRI analysis. *Front. Hum. Neurosci.* 7.

1252 Lau, J.C., Lerch, J.P., Sled, J.G., Henkelman, R.M., Evans, A.C., Bedell, B.J., 2008. Longitudinal
1253 neuroanatomical changes determined by deformation-based morphometry in a
1254 mouse model of Alzheimer's disease. *NeuroImage* 42 (1), 19–27.

1255 Lerch, J.P., Pruessner, J.C., Zijdenbos, A., Hampel, H., Teipel, S.J., Evans, A.C., 2005. Focal
1256 decline of cortical thickness in Alzheimer's disease identified by computational
1257 neuroanatomy. *Cereb. Cortex* 15 (7), 995–1001.

1258 Leung, K.K., Ridgway, G.R., Ourselin, S., Fox, N.C., Initiative, A.D.N., 2012. Consistent multi-
1259 time-point brain atrophy estimation from the boundary shift integral. *NeuroImage* 59
1260 (4), 3995–4005.

1261 Leung, K.K., Bartlett, J.W., Barnes, J., Manning, E.N., Ourselin, S., Fox, N.C., Initiative, A.D.N.,
1262 2013. Cerebral atrophy in mild cognitive impairment and Alzheimer disease: rates
1263 and acceleration. *Neurology* 80 (7), 648–654.

1264 Li, Y., Gilmore, J.H., Shen, D., Styner, M., Lin, W., Zhu, H., 2013. Multiscale adaptive gener-
1265 alized estimating equations for longitudinal neuroimaging data. *NeuroImage* 72,
1266 91–105.

1267 Littmann, A., Guehring, J., Buechel, C., Stiehl, H.-S., 2006. Acquisition-related morphologi-
1268 cal variability in structural MRI. *Acad. Radiol.* 13 (9), 1055–1061.

1269 Lorenzi, M., Pennec, X., 2013. Efficient parallel transport of deformations in time series of
1270 images: from Schild's to pole ladder. *J. Math. Imaging Vision* 50 (1–2), 5–17.

1271 McArdle, J.J., 2009. Latent variable modeling of differences and changes with longitudinal
1272 data. *Annu. Rev. Psychol.* 60, 577–605.

1273 Misra, C., Fan, Y., Davatzikos, C., 2009. Baseline and longitudinal patterns of brain atrophy
1274 in MCI patients, and their use in prediction of short-term conversion to AD: results
1275 from ADNI. *NeuroImage* 44 (4), 1415–1422.

1276 Moffat, S.D., Szekely, C.A., Zonderman, A.B., Kabani, N.J., 2000. Longitudinal change in
1277 hippocampal volume as a function of apolipoprotein E genotype. *Neurology* 55 (1),
1278 134–136.

1279 Morgen, K., Frölich, L., Tost, H., Plichta, M.M., Kölsch, H., Rakebrandt, F., Rienhoff, O., Jessen,
1280 F., Peters, O., Jahn, H., Luckhaus, C., Hüll, M., Gertz, H.-J., Schröder, J., Hampel, H.,
1281 Teipel, S.J., Pantel, J., Heuser, I., Wiltfang, J., Rütger, E., Kornhuber, J., Maier, W.,
1282 Meyer-Lindenberg, A., 2013. APOE-dependent phenotypes in subjects with mild cog-
1283 nitive impairment converting to Alzheimer's disease. *J. Alzheimer Res.* 37 (2),
1284 389–401.

1285 Mueller, S.G., Weiner, M.W., Thal, L.J., Petersen, R.C., Jack, C.R., Jagust, W., Trojanowski, J.Q.,
1286 Toga, A.W., Beckett, L., 2005. Ways toward an early diagnosis in Alzheimer's disease:

- 1287 the Alzheimer's Disease Neuroimaging Initiative (ADNI). *Alzheimers Dement.* 1 (1),
1288 55–66.
- 1289 Penny, W.D., 2012. Comparing dynamic causal models using AIC, BIC and free energy.
1290 *NeuroImage* 59 (1), 319–330.
- 1291 Penny, W.D., Ridgway, G.R., 2013. Efficient posterior probability mapping using Savage-
1292 Dickey ratios. *PLoS One* 8 (3), e59655.
- 1293 Penny, W.D., Stephan, K.E., Mechelli, A., Friston, K.J., 2004. Comparing dynamic causal
1294 models. *NeuroImage* 22 (3), 1157–1172.
- 1295 Pudas, S., Persson, J., Josefsson, M., de Luna, X., Nilsson, L.-G., Nyberg, L., 2013. Brain char-
1296 acteristics of individuals resisting age-related cognitive decline over two decades.
1297 *J. Neurosci.* 33 (20), 8668–8677.
- 1298 Raz, N., Lindenberger, U., 2011. Only time will tell: Cross-sectional studies offer no solu-
1299 tion to the age–brain–cognition triangle: Comment on Salthouse (2011). *Psychol.*
1300 *Bull.* 137 (5), 790–795.
- 1301 Raz, N., Rodrigue, K.M., 2006. Differential aging of the brain: patterns, cognitive correlates
1302 and modifiers. *Neurosci. Biobehav. Rev.* 30 (6), 730–748.
- 1303 Raz, N., Lindenberger, U., Rodrigue, K.M., Kennedy, K.M., Head, D., Williamson, A., Dahle,
1304 C., Gerstorff, D., Acker, J.D., 2005. Regional brain changes in aging healthy adults: gen-
1305 eral trends, individual differences and modifiers. *Cereb. Cortex* 15 (11), 1676–1689.
- 1306 Raz, N., Ghisletta, P., Rodrigue, K.M., Kennedy, K.M., Lindenberger, U., 2010. Trajectories of
1307 brain aging in middle-aged and older adults: regional and individual differences.
1308 *NeuroImage* 51 (2), 501–511.
- 1309 Raznahan, A., Lerch, J.P., Lee, N., Greenstein, D., Wallace, G.L., Stockman, M., Clasen, L.,
1310 Shaw, P.W., Giedd, J.N., 2011a. Patterns of coordinated anatomical change in human
1311 cortical development: a longitudinal neuroimaging study of maturational coupling.
1312 *Neuron* 72 (5), 873–884.
- 1313 Raznahan, A., Shaw, P.W., Lalonde, F., Stockman, M., Wallace, G.L., Greenstein, D., Clasen,
1314 L., Gogtay, N., Giedd, J.N., 2011b. How does your cortex grow? *J. Neurosci.* 31 (19),
1315 7174–7177.
- 1316 Raznahan, A., Shaw, P.W., Lerch, J.P., 2014. Longitudinal four-dimensional mapping of
1317 subcortical anatomy in human development. *Proc. Natl. Acad. Sci. U. S. A.*
- 1318 Resnick, S.M., Goldszal, A.F., Davatzikos, C., Golski, S., Kraut, M.A., Metter, E.J., Bryan, R.N.,
1319 Zonderman, A.B., 2000. One-year age changes in MRI brain volumes in older adults.
1320 *Cereb. Cortex* 10 (5), 464–472.
- 1321 Reuter, M., Fischl, B., 2011. Avoiding asymmetry-induced bias in longitudinal image
1322 processing. *NeuroImage* 57 (1), 19–21.
- 1323 Reuter, M., Rosas, H.D., Fischl, B., 2010. Highly accurate inverse consistent registration: a
1324 robust approach. *NeuroImage* 53 (4), 1181–1196.
- 1325 Reuter, M., Schmansky, N.J., Rosas, H.D., Fischl, B., 2012. Within-subject template estima-
1326 tion for unbiased longitudinal image analysis. *NeuroImage* 61 (4), 1402–1418.
- 1327 Risacher, S.L., Shen, L., West, J.D., Kim, S., McDonald, B.C., Beckett, L.A., Harvey, D.J., Jack,
1328 C.R., Weiner, M.W., Saykin, A.J., the Alzheimer Disease Neuroimaging Initiative,
1329 2010. Longitudinal MRI atrophy biomarkers: relationship to conversion in the ADNI
1330 cohort. *Neurobiol. Aging* 31 (8), 1401–1418.
- 1331 Rosa, M.J., Bestmann, S., Harrison, L., Penny, W., 2010. Bayesian model selection maps for
1332 group studies. *NeuroImage* 49 (1), 217–224.
- 1333 Sabuncu, M.R., Bernal-Rusiel, J.L., Reuter, M., Greve, D.N., Fischl, B., for the Alzheimer's Dis-
1334 ease Neuroimaging Initiative, 2014. Event time analysis of longitudinal neuroimage
1335 data. *NeuroImage* <http://dx.doi.org/10.1016/j.neuroimage.2014.04.015>.
- 1336 Schmid, V.J., Whitcher, B., Padhani, A.R., Taylor, N.J., Yang, G.-Z., 2009. A Bayesian
1337 hierarchical model for the analysis of a longitudinal dynamic contrast-enhanced
1338 MRI oncology study. *Magn. Reson. Med.* 61 (1), 163–174.
- 1339 Schnaudigel, S., Preul, C., Ugur, T., Mentzel, H.J., Witte, O.W., Tittgemeyer, M., Hagemann,
1340 G., 2010. Positional brain deformation visualized with magnetic resonance
1341 morphometry. *Neurosurgery* 66 (2), 376–384.
- 1342 Schumann, C.M., Bloss, C.S., Barnes, C.C., Wideman, G.M., Carper, R.A., Akshoomoff, N.,
1343 Pierce, K., Hagler, D., Schork, N., Lord, C., Courchesne, E., 2010. Longitudinal magnetic
1344 resonance imaging study of cortical development through early childhood in autism. *J.*
1345 *J. Neurosci.* 30 (12), 4419–4427.
- 1346 Schwartzman, A., Dougherty, R.F., Lee, J., Ghahremani, D., Taylor, J.E., 2009. Empirical null
1347 and false discovery rate analysis in neuroimaging. *NeuroImage* 44 (1), 71–82.
- 1348 Shaw, P.W., Greenstein, D., Lerch, J.P., Clasen, L., Lenroot, R., Gogtay, N., Evans, A.C.,
1349 Rapoport, J., Giedd, J.N., 2006. Intellectual ability and cortical development in children
1350 and adolescents. *Nature* 440 (7084), 676–679.
- 1351 Shaw, P.W., Kabani, N.J., Lerch, J.P., Eckstrand, K., Lenroot, R., Gogtay, N., Greenstein, D.,
1352 Clasen, L., Evans, A.C., Rapoport, J.L., Giedd, J.N., Wise, S.P., 2008. Neurodevelopmental
1353 trajectories of the human cerebral cortex. *J. Neurosci.* 28 (14), 3586–3594.
- 1354 Skup, M., Zhu, H., Zhang, H., 2012. Multiscale adaptive marginal analysis of longitudinal
1355 neuroimaging data with time-varying covariates. *Biometrics* 68 (4), 1083–1092.
- 1356 Smith, A.D., Smith, S.M., de Jager, C.A., Whitbread, P., Johnston, C., Agacinski, G., Oulhaj, A.,
1357 Bradley, K.M., Jacoby, R., Refsum, H., 2010. Homocysteine-lowering by B vitamins
1358 slows the rate of accelerated brain atrophy in mild cognitive impairment: a random-
1359 ized controlled trial. *PLoS One* 5 (9), e12244.
- 1360 Taki, Y., Thyreau, B., Kinomura, S., Sato, K., Goto, R., Wu, K., Kawashima, R., Fukuda, H.,
1361 2013. A longitudinal study of the relationship between personality traits and the an-
1362 nual rate of volume changes in regional gray matter in healthy adults. *Hum. Brain*
1363 *Mapp.* 34 (12), 3347–3353.
- 1364 Taylor, J.L., Scanlon, B.K., Farrell, M., Hernandez, B., Adamson, M.M., Ashford, J.W., Noda, A.,
1365 Murphy, G.M., Weiner, M.W., 2014. APOE-epsilon4 and aging of medial temporal lobe
1366 gray matter in healthy adults older than 50 years. *Neurobiol. Aging* <http://dx.doi.org/10.1016/j.neurobiolaging.2014.05.011>.
- 1367 Thambisetty, M., An, Y., Kinsey, A., Koka, D., Saleem, M., Guentert, A., Kraut, M., Ferrucci, L.,
1368 Davatzikos, C., Lovestone, S., Resnick, S.M., 2012. Plasma clusterin concentration is as-
1369 sociated with longitudinal brain atrophy in mild cognitive impairment. *NeuroImage*
1370 59 (1), 212–217.
- 1371 Tosun, D., Schuff, N., Truran-Sacrey, D., Shaw, L.M., 2010. Relations between brain tissue
1372 loss, CSF biomarkers, and the ApoE genetic profile: a longitudinal MRI study.
1373 *Neurobiol. Aging* 31 (8), 1340–1354.
- 1374 Vemuri, P., Wiste, H.J., Weigand, S.D., Knopman, D.S., Shaw, L.M., Trojanowski, J.Q., Aisen,
1375 P.S., Weiner, M., Petersen, R.C., Jack, C.R., Initiative, A.D.N., 2010a. Effect of apolipoprotein
1376 E on biomarkers of amyloid load and neuronal pathology in Alzheimer disease.
1377 *Ann. Neurol.* 67 (3), 308–316.
- 1378 Vemuri, P., Wiste, H.J., Weigand, S.D., Knopman, D.S., Trojanowski, J.Q., Shaw, L.M.,
1379 Bernstein, M.A., Aisen, P.S., Weiner, M., Petersen, R.C., Jack, C.R., Initiative, A.D.N.,
1380 2010b. Serial MRI and CSF biomarkers in normal aging, MCI, and AD. *Neurology* 75
1381 (2), 143–151.
- 1382 Woolrich, M.W., 2012. Bayesian inference in fMRI. *NeuroImage* 62 (2), 801–810.
- 1383 Young, A.L., Oxtoby, N.P., Daga, P., Cash, D.M., Fox, N.C., Ourselin, S., Schott, J.M., Alexander,
1384 D.C., Initiative, A.D.N., 2014. A data-driven model of biomarker changes in sporadic
1385 Alzheimer's disease. *Brain* 137 (Pt 9), 2564–2577.
- 1386 Ziegler, G., Dahnke, R., Gaser, C., the Alzheimer Disease Neuroimaging Initiative, 2012a.
1387 Models of the aging brain structure and individual decline. *Front. Neuroinformatics* 6, 3.
1388 Ziegler, G., Dahnke, R., Jäncke, L., Yotter, R.A., May, A., Gaser, C., 2012b. Brain structural tra-
1389 jectories over the adult lifespan. *Hum. Brain Mapp.* 33, 2377–2389.
- 1390 Ziegler, G., Dahnke, R., Winkler, A.D., Gaser, C., 2013. Partial least squares correlation of
1391 multivariate cognitive abilities and local brain structure in children and adolescents.
1392 *NeuroImage* 82, 284–294.
- 1393 Ziegler, G., Ridgway, G.R., Dahnke, R., Gaser, C., ADNI, A.D.N.I., 2014. Individualized Gauss-
1394 ian process-based prediction and detection of local and global gray matter abnormal-
1395 ities in elderly subjects. *NeuroImage* 97, 333–348.